UNIVERSITÀ DEGLI STUDI DI MODENA E REGGIO EMILIA

Dipartimento di
Ingegneria Enzo Ferrari
PhD Degree in Ingegneria Industriale e del Territorio

PhD Thesis

Stability analysis of in–plane modes of racing motorcycles employing symbolic algebra multibody modeling

Advisor:
Prof. Silvio Sorrentino

Candidate:
Stefano Cattabriga

Academic year 2019-2020

Contents

Introduction **1**

1 State of the art **3**
- 1.1 Stability of single–track vehicles 3
- 1.2 Stability of the motorcycle system 4
- 1.3 Chatter 5
- 1.4 Patter of the front wheel 7

2 Driveline instability **9**
- 2.1 Model description 11
- 2.2 Model linearization 14
- 2.3 Manoeuvre description 18
- 2.4 Analysis of the unstable phenomenon 20
- 2.5 Frozen-time eigenvalue analysis 25
- 2.6 Stability threshold 29
- 2.7 Comparison with a simplified model 33
  - 2.7.1 Simplified model parameters 34
  - 2.7.2 Comparison between the two models 35

3 Front wheel patter instability **39**
- 3.1 Minimal model 41
  - 3.1.1 Description of the model 41
  - 3.1.2 Non–linear equations of motion 43
  - 3.1.3 Linearized constitutive equation of the longitudinal ground force 44
  - 3.1.4 Linearized equations of motion 46
- 3.2 Stability analysis 48
  - 3.2.1 Stability maps 48

3.2.2 Comparison with a multibody planar motorcycle model 53
3.2.3 The unstable mode 56
3.2.4 Analysis of the source of instability 58

Conclusions 67

A 71

A.1 Full multibody model description 71
  A.1.1 Motorcycle model geometry 71
  A.1.2 Geometric parameters 72
  A.1.3 Independent coordinates 72
  A.1.4 Closure equation 73
  A.1.5 Rigid bodies 73
  A.1.6 Controls 74
  A.1.7 Internal forces and torques 75
  A.1.8 External forces and torques 76
  A.1.9 Rigid ring tyre model 77
  A.1.10 Magic Formula 78
  A.1.11 Transmission model 79
  A.1.12 Modifications to the full multibody employed in front patter analysis 82

B 87

B.1 Parameters adopted for the driveline stability analysis 87
B.2 Parameters adopted for the patter stability analysis 89

Bibliography 93

Introduction

Experimental evidence shows that road racing motorcycles are often subject to peculiar stability issues [1], which commonly arise due to the high stresses that all mechanical parts and systems suffer in this kind of vehicles. These events generally consist of self–excited vibrations, which involve one or more elements of the motorcycle. Several studies can be found in the literature on this subject, dealing with different instability phenomena, e.g. chatter, weave, wobble, front wheel patter [1, 2, 3]. Each of them can be identified with a mode of vibration of the motorcycle, with its own typical frequency and modal shape, which can be reproduced by suitable multibody models. The aim of this work is to identify the switching mechanisms of some of these self–excited vibrations, focusing on the in–plane modes of the motorcycle. To this purpose, novel tools for stability analysis are employed, along with root loci and time domain simulations, which have a wider documented use in the literature [4]. In particular, a numerical algorithm is developed for computing stability maps descending from symbolic algebra multibody models.

In this thesis the two main instability mechanisms that affect the motorcycle longitudinal dynamics are studied, the so–called "chatter" of rear wheel and "patter" of front wheel, both of them consisting of self–excited vibrations which can arise during heavy braking in straight motion. In both kinds of motion, the out–of–plane components are negligible, or they are not a necessary condition to the onset of instability [5], hence planar multibody models are employed, with rigid bodies. The full motorcycle multibody models employed in this work feature all the relevant moving parts of the vehicle, therefore they are suitable to carry on transient manoeuvres in the time domain. The stability of these models is studied next to modal analysis of reduced or simplified models with the lowest possible number of degrees of freedom. These minimal models represent sub–systems of the vehicle, since they are designed in order to capture the essential characteristics of the specific instability mechanism under study, taking into account only the elements which are necessary to the onset of the self–excited vibrations. Taking advantage of the simplicity of these models, the equations of motion are linearized in steady–state conditions, and the system matrices are analyzed to highlight the crucial parameters that can bring the actual vehicle to instability.

Experience of race engineers and riders confirms that in motorcycles all kinds of instability are always to prevent, since they weaken the vehicle overall performance, due to the severe oscillations of the tyre–ground vertical loads that can arise, causing a loss of grip and making the vehicle harder to control [6]. The results of the present work give a comprehensive description of the in–plane instability phenomena of a racing motorcycle, highlighting the parameters that play a key role in the onset of chatter and patter vibrations. In particular, the geometry of the rear (swing–arm) and front (telescopic fork) suspensions are demonstrated to have major role in the unstable phenomena, together with their damping and stiffness. The roles of the chain transmission and of the structural compliance of the frame and the forks are also studied. These results can be useful to prevent instability, by careful design of the motorcycle elements, by the correct choice of stiffness and damping parameters or by introduction of new devices on the vehicle.

Chapter 1

State of the art

1.1 Stability of single–track vehicles

The stability of single–track vehicles has been a research topic even from the early start of the motorization era. The first works on this topic date back to the last years of 19th century, with contribution from McGaw [7] and Whipple [8]. The latter developed a mathematical model that is still the basis of many research works. In the following decades, the research was pushed by the need to find solutions to practical issues arising from the increasing speed and complexity of the contemporary motorcycles. In those years, the practical implications of the unstable modes of the motorcycle have been studied mainly by industrial publications, e.g. [9]. In the 70s and 80s the research on the motorcycle stability saw an acceleration, with major contributions from Sharp [10], who helped to define the approach of the modern works on the topic developing a model for the free–control motorcycle. This work gave a summary of the modes of the motorcycle, highlighting the ones that can be unstable in constant speed conditions: capsize, weave, wobble, also clarifying that the wobble is impossible to obtain if tyre sideslip is inhibited. From this moment on, the research on the motorcycle dynamics expanded in many different directions. Some authors developed the branch of the rider control topic, dealing more with handling than stability ([11, 12, 13]). Those authors that continued to focus on the stability topic, in some cases abandoned the idea of rigid bodies, to come to the conclusion that some forms of frame compliance have an important role in destabilizing the vehicle, as the torsional compliance does with the wobble mode [14, 15, 16, 17, 18].

It was not until the last few decades, after the development of more sophisticated computer–aided simulation techniques [19], that authors started dealing with the stability issues of high performance racing motorcycles [20]. The renovated interest in this kind of vehicles led to publishing of works dealing with stability issues that were unmentioned in the literature before, e.g. chatter [1].

The latest works on motorcycle dynamics are more focused in finding computationally efficient ways to simulate the vehicle motion, and the complexity of the models has often made it difficult to find the root cause of the unstable phenomena of high performance motorcycles. This works focuses on simplicity, and aims at describing the switching mechanism of instabilities, showing that some kinds of instability are not necessarily a three dimensional problem.

1.2 Stability of the motorcycle system

The motorcycle system has been extensively studied in the scientific literature. Several models have been developed to study the dynamics of motorcycle, and more in general of the single–track vehicles. The topic of stability analysis consists in the study of the eigenvalue problem of the model, hence in the identification of the modes of the motorcycle. Unlike four–wheeled vehicles, the single–tracked ones exhibit several modes which can become unstable.

For an uncontrolled motorcycle model running straight ahead on a flat surface, the most common mode which can be unstable, especially at low speed, is the so–called capsize mode [21]. Mathematically, this is an instability of divergent type (i.e. non–oscillatory); physically, it represents the vehicle leaning on one side under the influence of gravity. Everyone has experienced the feeling of this mode when learning to ride a bicycle.

All other well–known motorcycle modes are of oscillatory type; some of these modes are substantially an in–plane motion, hence the movements of the motorcycle parts have negligible components in the direction perpendicular to the middle plane of the vehicle. One of the most common of these modes is the pitching, which consists mainly of the rotation of the sprung masses about an axis perpendicular to the middle plane. The second is the bounce mode, where the sprung masses have a primarily vertical motion, and the suspensions are compressed and extended simultaneously, as opposed to the pitching, where they have alternate compression and extension [4]. Finally, in–plane modes can be identified involving primarily the unsprung masses, which are often referred to as front hop and rear hop [22]. In these modes, either the front or rear unsprung mass oscillates vertically, while the rest of the vehicle remains almost stationary. Not all the motorcycle modes are in–plane, but some modes involve motions outside of the middle plane of the vehicle. This is the case of the weave mode [2], where the vehicle has an oscillatory roll motion and hence moves forward in a swinging movement. One other notorious anti–symmetrical mode is the wobble [20], which consist primarily in a steering oscillation, while the rear end of the vehicle stays still or slightly rolls on the sides.

The described modes are generally present in all kinds of motorcycle, and they can potentially be harmful for road riders. This work stresses the attention on other kinds of motion, which appear mainly in high performance racing motorcycles. Hence, the literature has started being interested in them only at a later time in history. This work focuses on the chatter and front wheel patter of the motorcycle, and analyses them in an in–plane approach, trying to give a physical explanation of these dangerous phenomena.

1.3 Chatter

The academic interest in the chatter phenomenon started around year 2000, with researches driven mainly by industrial interest in the phenomenon [23]. Various descriptions of the phenomenon were given in the literature; the more classical ones are mainly the scientific interpretation of the comments coming directly from the riders' experience. People in the field of motorcycle racing used to describe this phenomenon as an oscillation of the rear end of the vehicle starting during braking or when entering a corner. As many authors reported, measurements on instrumented vehicles showed that the frequency of such oscillation usually falls in the 17–22 Hz [1]. The first publications on the topic focused more on interpretation of the experimental data [1, 23] than on the investigation of the physical source of the phenomenon, even though many interesting insights were given. In particular, Cossalter was probably the first author to catch the essence of the chatter as described by the experienced workers of the racing industry. He identified the chatter vibration with that of an unstable mode involving primarily the powertrain of the motorcycle, and in a following publication [24] he made an extensive parametric analysis to show what vehicle characteristics and driving styles are most influential on the destabilization of this mode. However, the first article by Cossalter tried to explain the physical source of self excitation of chatter with an energy balance based on the detachment of the wheel by the road surface, while later on other authors [25] demonstrated that this is not a necessary condition for the onset of self excitation. There appears to be several uncertainties on the definition of chatter, since the first publications stated it appears when the throttle is closed and the braking phase has ended, i.e. in cornering, right before the throttle is reopened again. At the same time, planar models disregarding the lateral dynamics were used to study the phenomenon [1]. Other authors stated that chatter occurs in corner entry phase, thus included the braking force in the model they used to study the phenomenon [26]. At a later time, Sharp [27] allowed a three–dimensional interpretation of the phenomenon, but disregarded the presence of brake force applied. His conclusions led him to the discovery of a potentially unstable mode that he called "chatter", which in fact is in the frequency range of the experimentally highlighted phenomenon. Nonetheless, this mode involved mainly the front frame vibrating in steer and camber, being substantially related to the torsional frame flexibility, and it affected the rear end of the motorcycle to a minimum extent; this suggests that a more appropriate name for the mode discovered by Sharp could be "front chatter", whose existence had already been argued by Cossalter in [24], since it involves mainly the front end of the vehicle. On the physical interpretation of the chatter phenomenon, [28] was the first publication to deal in depth with the tyre characteristic function, but perhaps the most complete work on the chatter topic was published by Leonelli et al. in [6]. Here, three models of increasing complexity were developed to study the chatter phenomenon. In the most complex model, both the presence of roll angle and braking force are allowed. This work gave an important contribution to the understanding of the phenomenon, since it highlighted that its physical source could reside in the tyre characteristic, in particular in the partial derivative of the longitudinal force w.r.t. the slip. In this work it was showed that, since the tyre is operating near its limit adherence when chatter occurs, a negative value of said partial derivative can be a source of instability. Later works of the same authors focused on the investigation of this specific aspect, finally showing that a low value, still positive, of this parameter can be sufficient to the onset of chatter. In [5] it was pointed out that the negative value of the partial derivative would give source to a divergent type of instability, while the most influential parameter in determining the oscillating instability that can be associated to chatter is the partial derivative of the longitudinal ground force with respect to the vertical load.

1.4 Patter of the front wheel

The scientific research on the topic of front wheel patter has produced less publications than the chatter, even though the interest in this phenomenon has been developed earlier in history. The patter phenomenon can be described as a self–excited oscillation of the front wheel in the vertical and horizontal directions, associated to oscillation of the wheel angular velocity in a 7–10 Hz frequency range. This problem can occur especially in high performances motorcycles during heavy breaking manoeuvres in essentially straight line motion. The first and, to the author's knowledge, only article ever published specifically on front wheel patter dates back to 1983. In [3], Sharp and Giles employed an approach derived from the previous studies on axle tramp [29] to address the problem of front wheel patter in a two–dimensional way. Numerical simulation on the 4 degrees of freedom model developed led to the conclusion that the stability is improved by mismatching of the frequency of the forks pivoting on the frame compliance with the frequency of vertical motion of the wheel on the tyre and suspension springs. On the contrary, the tyre carcass (torsional) flexibility turned out to play a negligible role. The research developed in this work was enhanced by the intuition that the front wheel patter as described and studied by Sharp can sometimes be the precursor of the locking of the front wheel, since in the racing sector it has been observed that this phenomenon is often preceded by vibrations in the 7–10 Hz frequency range. The locking or sudden deceleration of the front wheel can have harmful consequences on the manoeuvrability of the vehicle and on the rider's safety, and this triggered the interest in the topic. It should also been mentioned that another phenomenon has been described by the name of "patter" in the literature. This also appeared in 1983, in the PhD thesis by Koenen [30]. In this work, the author discovered a mode than can become unstable in the case of free rolling during cornering at high roll angles, that originates from the merging of wobble and front hop due to the lateral dynamics. This phenomenon is significantly different from the patter as described by Sharp and as studied in this work; nevertheless, such interactions with lateral components at high roll angles are expected to be further modified when considering braking forces, representing a research subject left open to future investigations.

Chapter 2

Driveline instability

Introduction

The self–excited vibration often referred to as “chatter” is a recurrent phenomenon affecting the dynamics of modern road–racing motorcycles. The chatter vibration may show up (and it has been indeed observed) on the most diverse racing motorcycles, from two stroke lightweight machines [1] up to four stroke production–based vehicles [27], when driven on a dry racetrack at the limit of tyre adherence.

During the braking phase that anticipates the corner entry, the driver applies strong front brake force at a moderate roll angle, while the engine delivers engine brake torque due to closed throttle. In this condition, a vertical oscillation of the rear unsprung mass may appear, usually with a frequency between 17 and 22 Hz, and sometimes even as low as 15 Hz. This vibration can be observed on the angular motion of the driveline as well, and then it transfers to the front wheel. It keeps on during the latter braking phase, when the rider is reducing the front brake force while increasing the roll angle. From the corner apex to the subsequent acceleration, when the rider starts applying engine torque again, the vibration quickly disappears.

The suspensions are generally not able to dampen this kind of vibration, which cause severe fluctuations of the tyre–ground vertical load. As a consequence, when chatter occurs, the confidence of the rider drops: it becomes more difficult to estimate the available tyre adherence, thus preventing from achieving the maximum possible longitudinal and lateral accelerations. Therefore performance during braking and turning is seriously affected, leading to poor lap times, and the risk of crashing is increased.

Several contributions about this topic have been presented in the literature, but a definitive explanation of the phenomenon has not been given yet. In fact, a number of authors considered the problem as planar and focused on the interaction between driveline and rear tyre during braking manoeuvres, while others analyzed the stability of a three–dimensional motorcycle model during steady state cornering manoeuvres.

More precisely, Tezuka et al. [23] showed how an out–of–plane mode related to lateral and radial deformability of tyres may become unstable when increasing the cornering effort in steering pad manoeuvres. Sharp [27] demonstrated that the frame lateral and torsional flexibilities may give rise to an out–of–plane unstable mode in a frequency range close to the chatter one. On the other hand, Cossalter et al. [1, 24, 31] found that the driveline mode can become unstable during a straight running braking manoeuvre, due to interaction between chain and rear tyre when the latter loses contact with the track surface. Finally, in [25, 5] it has been shown how the actual values assumed by the rear tyre slip stiffness during a braking manoeuvre may yield instability in the driveline mode of a simplified planar model.

Starting from these results, in this study a planar (2D) model is considered, in order to analyze the influence of the tyre characteristic parameters on the stability of the driveline mode of a four stroke racing motorcycle. The stability is studied by means of both time domain simulations and frozen–time eigenvalue analysis. In order to extend the validity of eigenvalue analysis to transient, time–varying conditions, specific stationary braking manoeuvres are considered, making it possible to obtain stability maps of the model with respect to the tyre characteristic parameters.

The analysis of the above described phenomenon will be carried out in the following sections as follows. Sections 2.1 and 2.2 provide an overview of the vehicle model as long as a description of the corresponding vibration modes and related modal shapes. In Section 2.3 a braking manoeuvre measured on an instrumented test vehicle is simulated in the time domain, discussing the arising self–excited vibration. Section 2.4 describes a possible explanatory driving mechanism for the observed self–excited phenomenon. In Section 2.5 the behaviour of the time domain simulation is compared in terms of stability with the results coming from a corresponding frozen–time eigenvalue analysis, and a specific stationary manoeuvre is introduced. In Section 2.6, eigenvalue analysis is applied to the time–invariant system, and stability maps are drawn. Finally, in Section 2.7, the results of the analysis of the full non–linear model are compared and discussed with respect to those of the simplified linear 2 dofs model presented in [5].

2.1 Model description

A two–dimensional multibody motorcycle model is adopted, featuring planar rigid–ring tyres with Magic Formula (MF), chain transmission for both braking and traction phases, and full drivetrain inertia. A brief description of the model is given in this section, while a more detailed explanation is found in Appendix A, from Section A.1.1 to A.1.11.

The model, as sketched in Figure A.1, consists of eleven rigid bodies: main frame (including rider), swingarm, upper front assembly, lower front assembly, front and rear rims, front and rear tyre belts, and three bodies modelling the rotating inertias of crankshaft, main gearbox shaft (including clutch) and secondary gearbox shaft. The rider is considered fixed with respect to the main frame, in a braking configuration: the center of gravity (CoG) of the suspended mass and the aerodynamic coefficients are set accordingly.

The motorcycle geometry is described by means of three fixed parameters: the swingarm length l_{sa}, the frame length l_r, and the front fork offset l_f. The motorcycle internal configuration can be defined by means of two time dependent variables: the pitch angle α of the swingarm and the pitch angle μ of the frame line (correspondent to the actual caster angle), both defined with respect to the inertial reference system. The motorcycle kinematics are derived in a planar, ξ–forward, η–down reference system.

The front suspension elastic force is expressed as a function of h_f (geometric fork extension), by means of a tri–linear spring characteristic (modelling the main spring, the bottom–out bumper and the top-out spring). A nonlinear damping characteristic is also considered. The rear suspension is modelled with a non–linear torsional spring–damper system, on the basis of the relative angular displacement ζ between the frame line and the swingarm ($\zeta = \mu - \alpha$). Tri–linear spring and nonlinear damper characteristics are considered as well. The adopted characteristics for the front and rear dampers are reported in the appendix at Section A.1.7.

A standard rigid–ring model reduced in the wheel midplane generally presents three dofs: radial, longitudinal and torsional deformations. In the present study only the radial deformations β_f, β_r are considered: this allows

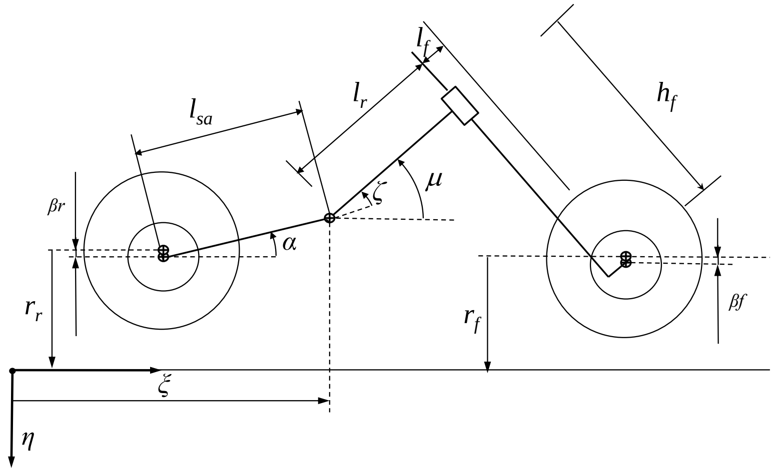

Figure 2.1: Schematic of the motorcycle model.

to obtain a more precise estimate of the tyre hop frequencies and the related modal shapes, while ensuring the correct overall tyre deformability. In fact, the rigid–ring torsional and longitudinal deformations may be neglected, since their associated stiffness (very high for road racing tyres) makes the contribution of the related modes negligible in the frequency range of interest. For the same reason, also the tyre relaxations have been neglected, due to the very low value of the associated relaxation lengths.

The actual tyre slip stiffness $C_\kappa = \frac{\partial F_\xi}{\partial \kappa}$ as well as $C_\eta = \frac{\partial F_\xi}{\partial F_\eta}$ are evaluated starting from the tyre force F_ξ, using the well–known Magic Formula approach [32]. In the proposed planar model, only the pure longitudinal tyre force F_ξ has to be considered. According to MF 6.2, its general expression reads:

$$F_\xi = D \sin(C \arctan(B\kappa - E(B\kappa - \arctan(B\kappa)))) \tag{2.1}$$

where the slip coefficient κ is evaluated using experimentally measured values for the tyre rolling radius as a function of the forward speed of the vehicle (as opposed to [24, 31] where the rolling radius is considered to be equal to the tyre deformed radius). In particular, coefficients B, C, D take into account

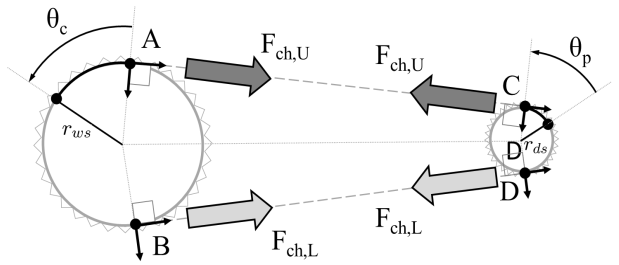

Figure 2.2: Schematic of the chain transmission model.

the dependency of the longitudinal force with the vertical load acting on the contact patch. Parameter D sets the maximum grip available, while the product BCD expresses the slope of the characteristic curve at the origin, in the form (considering unit scaling factors):

$$K_\xi = \left.\frac{\partial F_\xi}{\partial \kappa}\right|_{\kappa=0} = BCD = F_\eta (p_{Kx1} + p_{Kx2}\Delta F_\eta) e^{p_{Kx3}\Delta F_\eta} \tag{2.2}$$

where

$$\Delta F_\eta = \frac{(F_\eta - F_{\eta 0})}{F_{\eta 0}} \tag{2.3}$$

A quadratic as well as an exponential dependency on F_η is introduced by parameters p_{Kx2} and p_{Kx3}, whose effects will be shown in Section 2.4.

The adopted chain transmission model derives from the one presented in [25]. A schematic is presented in Figure 2.2, and a more extensive description of the chain model is given in Appendix A.1.11.

The chain force constitutive equation is based on a spring–damper system in parallel (Kelvin–Voigt). For this application, particular attention is needed when assessing the structural parameters of the transmission model, since it has been found that the associated mode may become unstable causing the chatter phenomenon [24, 31]. As a consequence, the total stiffness of the spring k_{tot} is evaluated taking into account the series composed by the chain (subscript c) and the sprocket torsional shock absorber (subscript ws), according to:

$$k_{tot} = \left(\frac{1}{k_c} + \frac{r_{ws}^2}{k_{ws}}\right)^{-1} \tag{2.4}$$

Table 2.1: Degrees of freedom of the proposed motorcycle model.

	Name	DoF
1	ξ	Pivot longitudinal displacement
2	μ	Frame line pitch
3	α	Swing arm pitch
4	θ_c	Rear wheel angular displacement
5	θ_p	Pinion angular displacement
6	θ_a	Front wheel angular displacement
7	r_r	Rear wheel deformed radius
8	r_f	Front wheel deformed radius
9	β_r	Rear rim-ring displacement
10	β_f	Front rim-ring displacement

The damping in the transmission may be assumed entirely due to the sprocket torsional absorber (considered linear), that is disregarding the internal damping of the chain. Hence the transmission damping c_{tot} can be expressed as:

$$c_{tot} = \frac{c_{ws}}{r_{ws}^2} \tag{2.5}$$

The degrees of freedom of the proposed model are described in Table 2.1. The equations of motion (EoMs) are obtained symbolically, by means of an open–source multibody library developed in Maple. The kinematic description makes it possible to evaluate the Lagrangian function L and to write the EoMs as:

$$\mathbf{M}(\mathbf{q})\ddot{\mathbf{q}} = -\mathbf{f}(\mathbf{q}, \ddot{\mathbf{q}}) \tag{2.6}$$

where $\mathbf{M}(\mathbf{q})$ denotes the mass matrix of the system and $\mathbf{f}(\mathbf{q}, \dot{\mathbf{q}})$ a vector containing all the terms proportional to displacements and velocities.

2.2 Model linearization

The system can be linearized considering a Taylor expansion of the EoMs for a selected configuration $\{\mathbf{q}_0, \dot{\mathbf{q}}_0\}$ as:

$$\mathbf{M}|_{\mathbf{q}_0}\ddot{\tilde{\mathbf{q}}} + \left.\frac{\partial \mathbf{f}_j}{\partial \dot{\mathbf{q}}_i}\right|_{\mathbf{q}_0, \dot{\mathbf{q}}_0} \cdot \dot{\tilde{\mathbf{q}}} + \left.\frac{\partial \mathbf{f}_j}{\partial \mathbf{q}_i}\right|_{\mathbf{q}_0, \dot{\mathbf{q}}_0} \cdot \tilde{\mathbf{q}} = \mathbf{0} \tag{2.7}$$

where $\tilde{\mathbf{q}} = \mathbf{q} - \mathbf{q}_0$. It can be noted that the second and third terms are the damping and stiffness matrices of the system:

$$\mathbf{C}(\mathbf{q}_0,\dot{\mathbf{q}}_0) = \left.\frac{\partial \mathbf{f}_j}{\partial \dot{\mathbf{q}}_i}\right|_{\mathbf{q}_0,\dot{\mathbf{q}}_0}, \quad \mathbf{K}(\mathbf{q}_0,\dot{\mathbf{q}}_0) = \left.\frac{\partial \mathbf{f}_j}{\partial \mathbf{q}_i}\right|_{\mathbf{q}_0,\dot{\mathbf{q}}_0} \tag{2.8}$$

The modal response is then estimated by numerically solving the associated generalized eigenvalue problem. In the Duncan state–space representation, the linearized EoMs become:

$$\underbrace{\begin{bmatrix} \mathbf{C} & \mathbf{M} \\ \mathbf{M} & \mathbf{0} \end{bmatrix}}_{\mathbf{A}} \begin{Bmatrix} \dot{\mathbf{q}} \\ \ddot{\mathbf{q}} \end{Bmatrix} + \underbrace{\begin{bmatrix} \mathbf{K} & \mathbf{0} \\ \mathbf{0} & -\mathbf{M} \end{bmatrix}}_{\mathbf{B}} \begin{Bmatrix} \mathbf{q} \\ \dot{\mathbf{q}} \end{Bmatrix} = \mathbf{0} \tag{2.9}$$

and the related eigenproblem reads:

$$(s\mathbf{A} + \mathbf{B})\mathbf{y} = \mathbf{0} \tag{2.10}$$

where s is the Laplace variable.

In order to describe the natural modes of the planar vehicle model, a series of constant speed manoeuvres are considered. The associated eigenvalues are shown in the root locus of Figure 2.3, where four modes can be identified: driveline, rear and front hop, bounce. Due to the suspension damping parameters chosen, the pitch mode results over–damped. Moreover, the two modes related to the rigid-ring radial deformations are located outside of the frequency range of interest (namely near 60 Hz). It is also noted that out of plane modes, such as weave and wobble, cannot be simulated with the adopted model since it does not feature neither roll nor steering dofs. Since all the eigenvalues of the time–invariant system have negative real part, the system shows asymptotically stable behaviour.

The increase with speed in both the real and the imaginary parts of the driveline eigenvalues can be explained considering the linearized expression of the rear tyre longitudinal force, which reads:

$$\tilde{F}_{\xi-r} = C_{\kappa-r}\tilde{\kappa} + C_{\eta-r}\tilde{F}_{\eta-r} = \left(\frac{C_{\kappa-r}}{V_{\xi-r}}\right)\tilde{V}_{s\xi-r} + C_{\eta-r}\tilde{F}_{\eta-r} \tag{2.11}$$

The values of $C_{\kappa-r}$ and $C_{\eta-r}$ can be considered constant, since the tyre is working in the linear part of its characteristic, due to the low thrust needed to maintain constant imposed speeds. Therefore, the equivalent damping

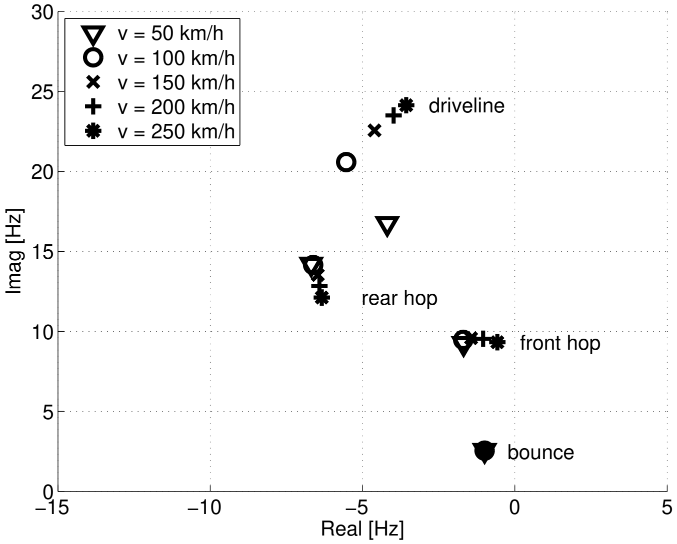

Figure 2.3: Root locus for constant speed manoeuvres.

in the tyre force model decreases with increasing speed, while all the other parameters remain constant.

The i-th state-space (complex) eigenvector $\mathbf{y}_i$ can be represented in the form:

$$\mathbf{y}_i = \left[\begin{array}{cc} \boldsymbol{\psi}_i & s_i\boldsymbol{\psi}_i \end{array} \right]^T \tag{2.12}$$

where $\boldsymbol{\psi}_i$ denotes the displacement eigenvector.

For display and comparison of the modal shapes $\boldsymbol{\psi}_i$, all the degrees of freedom quantities are made homogeneous to linear displacements. To achieve this, each of the rotational degrees of freedom is multiplied by an associated length, chosen in a meaningful way with respect to the physics of the vehicle model. The rotation angles of the driveline elements θ_c, θ_p, θ_a, are converted into longitudinal displacements of the tyres contact points according to:

$$\begin{gathered} \theta_c \rightarrow \theta_c R_r \\ \theta_p \rightarrow \theta_p \left(\frac{r_{ds}}{r_{ws}} \right) R_r \\ \theta_a \rightarrow \theta_a R_f \end{gathered} \tag{2.13}$$

where R_f and R_r are the radius of the front and rear wheel respectively. The frame pitch angle μ and the swingarm angle α are converted into vertical

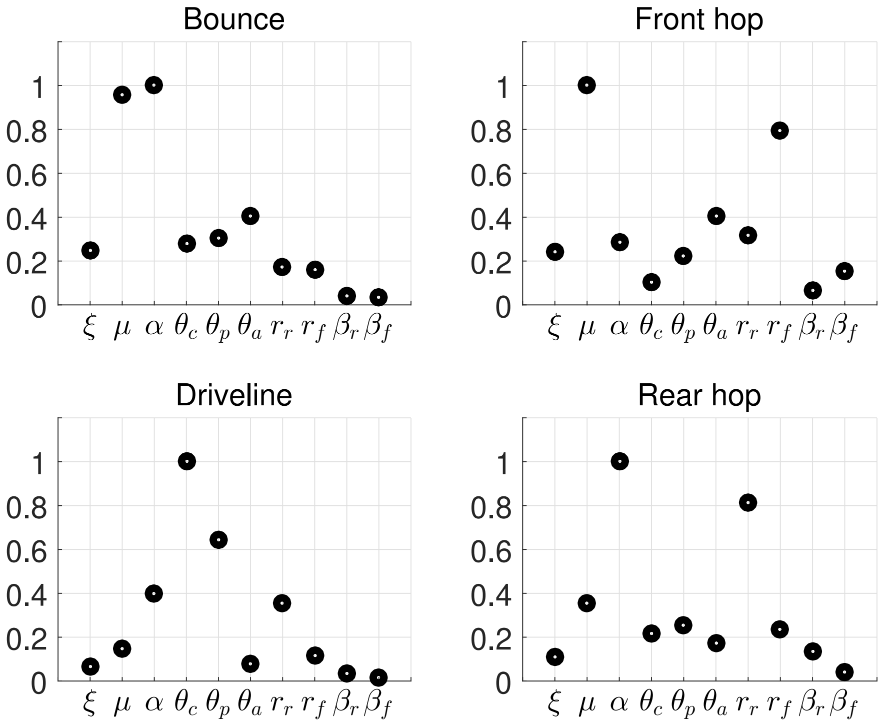
Bounce

Front hop

Driveline

Rear hop

Figure 2.4: Modal shapes at v = 100 km/h.

displacements at the front and rear wheel axles according to:

$$\begin{gathered} \alpha \rightarrow \alpha l_{sa} \cos(\alpha_0) \\ \mu \rightarrow \mu \left[(l_f + l_r) \cos(\mu_0) + h_{f0} \sin \mu_0 \right] \end{gathered} \tag{2.14}$$

where the subscript 0 indicates the value of each variable in the equilibrium configuration about which the linearization is performed.

The resulting transformed complex modal shapes can then be represented by plotting the absolute values of each component, normalized with respect to the maximum value (i.e. unit value of the maximum component of each eigenvector). Figure 2.4 shows the modal shapes at v = 100 km/h (in clockwise order: bounce, front hop, rear hop, and driveline).

It can be observed that the transmission mode features driveline angular oscillation coupled with swingarm pitch and rear tyre radial deformation.

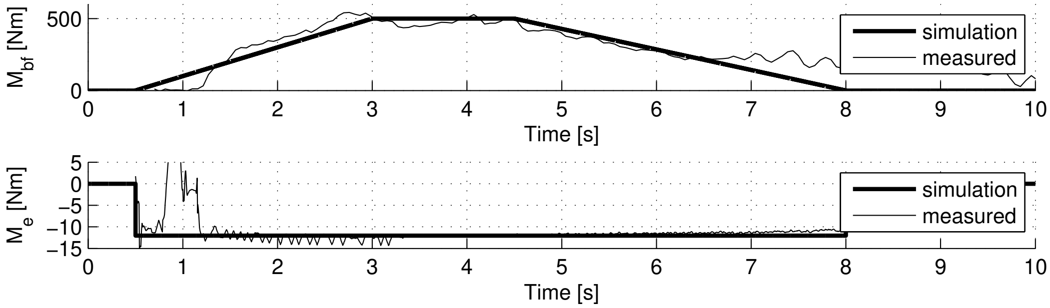

Figure 2.5: Controls for the braking manoeuvre. M_{bf}: front brake torque; M_e: engine torque.

2.3 Manoeuvre description

A typical profile for the applied controls M_{bf} (front brake torque) and M_e (engine torque) during a straight running braking manoeuvre can be inferred from experimental data measured from an instrumented test motorcycle, as shown in Figure 2.5. During the braking phase, the engine brake torque is set to a constant value: this is due to both the engine idle speed (braking is performed with closed throttle) and the torque threshold built in the slippery clutch (also known as anti–hop clutch). The front brake torque profile can be approximated with a tri–linear function of time, consisting of an initial ramp, a constant torque phase and a decreasing ramp. The rear brake, in general, is not activated during the initial, straight running braking phase, since the available force at the rear tyre is already saturated by the engine brake. Hence, the rear brake is not considered in the described manoeuvre, which is entirely performed using first gear. Initial conditions for the time domain integration consist of null controls and static equilibrium states.

The velocity and acceleration profiles resulting from time domain integration are shown in Figure 2.6. The maximum deceleration is -8.834 m/s^2, obtained at t = 2.999 s, while the velocity spans from 200 to 30 km/h.

An oscillation in the longitudinal acceleration can be observed at around 22 Hz between 4 and 5 s, fading away when the front brake torque starts decreasing. This acceleration oscillation is due to the longitudinal force of the rear tyre, as it can be seen in Figure 2.7, along with the vertical loads acting on the contact points.

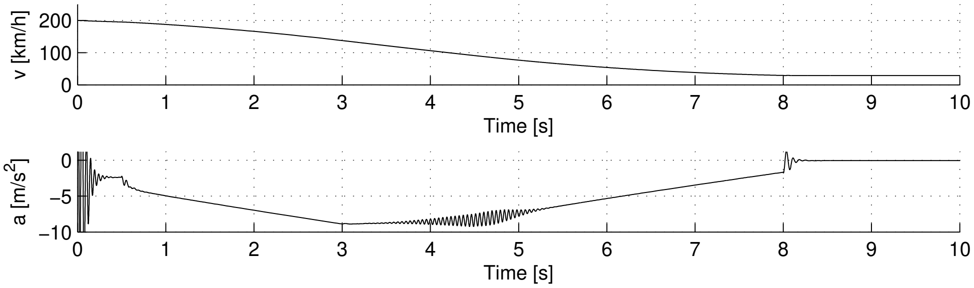

Figure 2.6: Velocity and acceleration profiles during the braking manoeuvre.

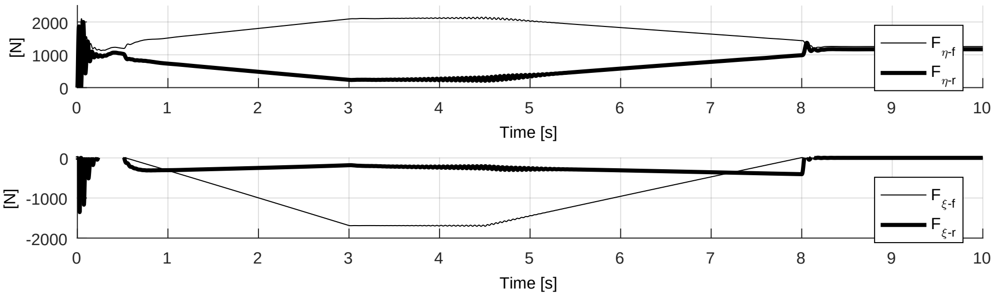

Figure 2.7: Front and rear vertical tyre forces (top) and longitudinal tyre forces (bottom) during the braking manoeuvre.

The severe weight transfer generated by the front brake torque loads the front tyre with over 2000 N at the deceleration peak, which means that most of the vehicle weight (see Appendix B.1) is supported by the front tyre. The rear tyre is therefore lightly loaded, but nevertheless subjected to a non-negligible engine brake torque. The minimum rear tyre load is 235.5 N, recorded at t = 3.03 s, when a small oscillation around the minimum value starts, and suddenly propagates to the front. The following phase relations can be observed at the vibration onset:

- counter–phase between pinion and wheel sprocket rotation (Figure 2.8);
- counter–phase between swingarm pitch and rear deformed tyre radius (Figure 2.8);
- in–phase between the rear vertical load and the (absolute) rear tyre longitudinal force;
- counter–phase between front and rear vertical load;
- in–phase between longitudinal acceleration and rear tyre force.

An oscillation at the same frequency is also present in the rear tyre longitudinal slip and slightly in the front tyre slip as shown in Figure 2.8. The slip variation is evident in the rear wheel angular oscillation as well which, in turn, is balanced by the force exerted by the lower segment of the chain, tight due to the engine brake torque. Therefore, the chain force exhibits the same 22 Hz oscillation, in–phase with the (absolute) longitudinal slip.

2.4 Analysis of the unstable phenomenon

The same oscillation observed for the rear slip, vertical and longitudinal tyre forces is also evident on the slip stiffness. Three points (peak–mid–minimum) taken from an increasing oscillation quasi–periods are marked in Figure 2.9, over their respective MF diagrams. It can be seen how the variation of vertical load modifies the shape of the tyre characteristic function, due to the dependence introduced by p_{Kx2} and p_{Kx3} (Eq. 2.2), giving rise to very different slip stiffness values. The (absolute) minimum C_κ is related to the minimum F_η, close to the F_ξ peak force. The maximum C_κ, on the other

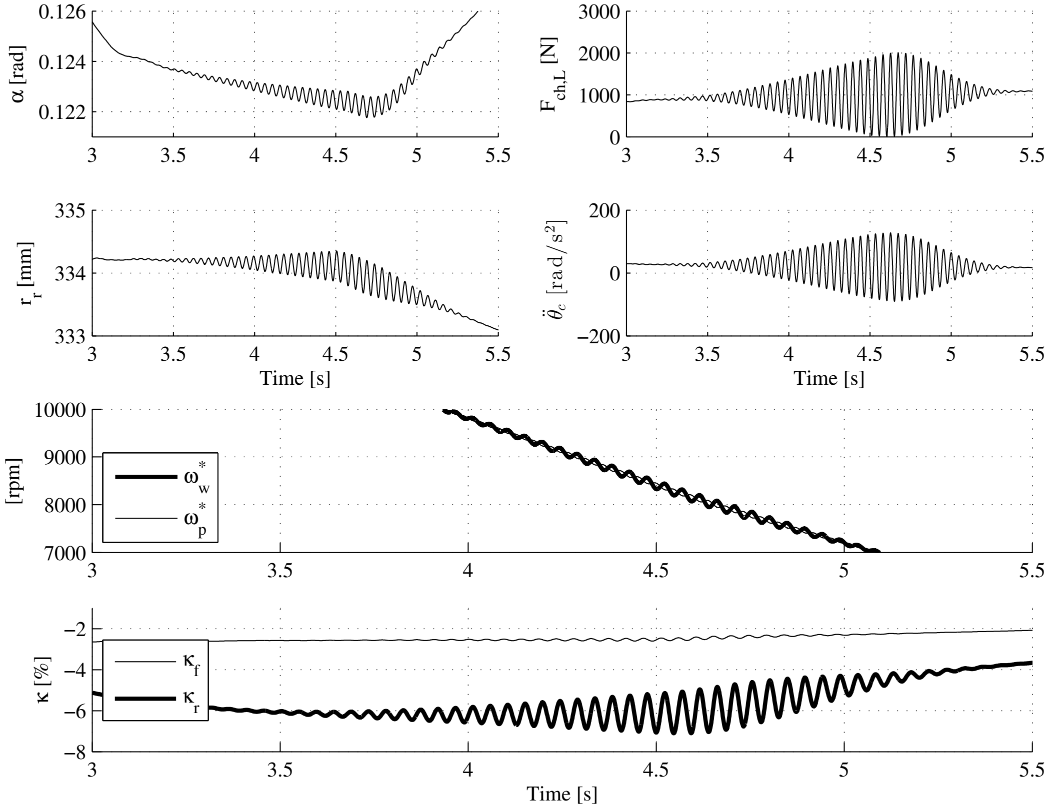

Figure 2.8: α: swingarm pitch; r_r: rear deformed radius; $F_{ch,L}$: chain force; $\ddot{\theta}_c$: rear wheel angular acceleration; ω_c^*, ω_p^*: rear wheel and pinion angular velocities reduced to the crankshaft; κ_r, κ_f: rear and front longitudinal slip.

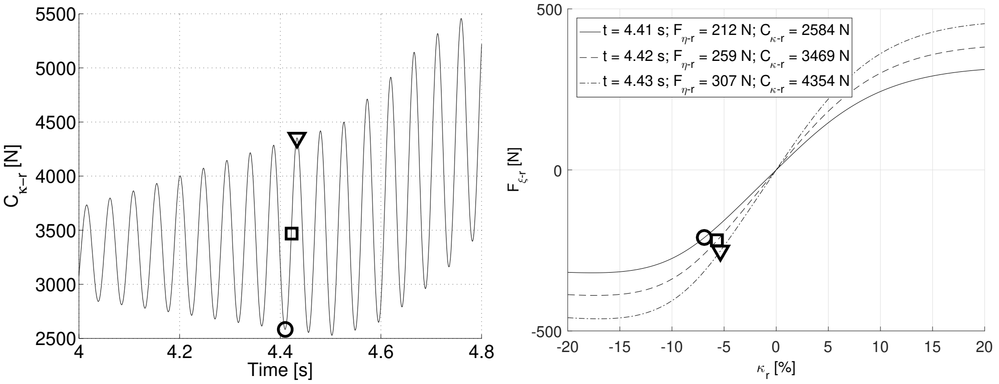

Figure 2.9: Rear tyre slip stiffness as a function of time (left), and MF for three conditions of minimum, mean and maximum C_κ (right).

hand, is associated with the maximum F_η reached during the oscillation quasi–period, and it is close to its value in the origin ($\kappa_r = 0$).

The evolution of the self–excited oscillation is now studied considering three quasi–periods at different times, evidenced in Figure 2.10 highlighting the phase–lags between vertical and longitudinal forces. During the first quasi–period (solid line) the amplitude is increasing, during the second one (dotted line) the maximum amplitude is reached, and during the third one (dash–dotted line) the oscillation is fading away. Time spans in the ranges 3.705–3.755 s, 4.680–4.730 s, 5.015–5.065 s respectively.

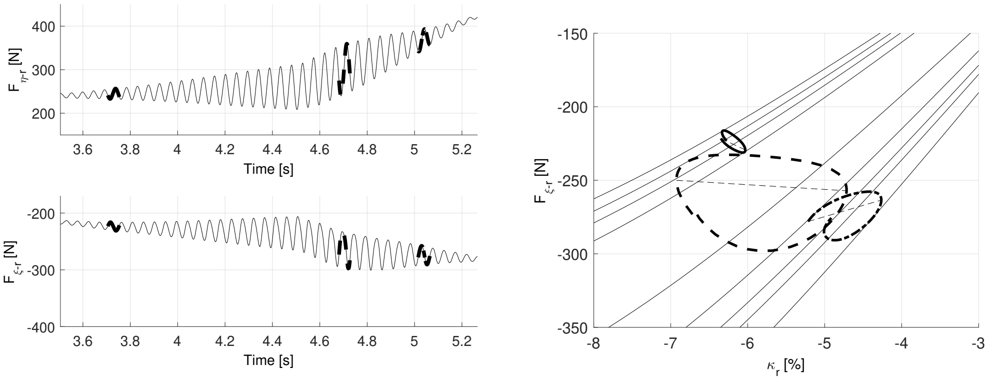

Figure 2.10: Rear tyre forces (left) and oscillation quasi–periods in the κ_r-F_ξ plane (right).

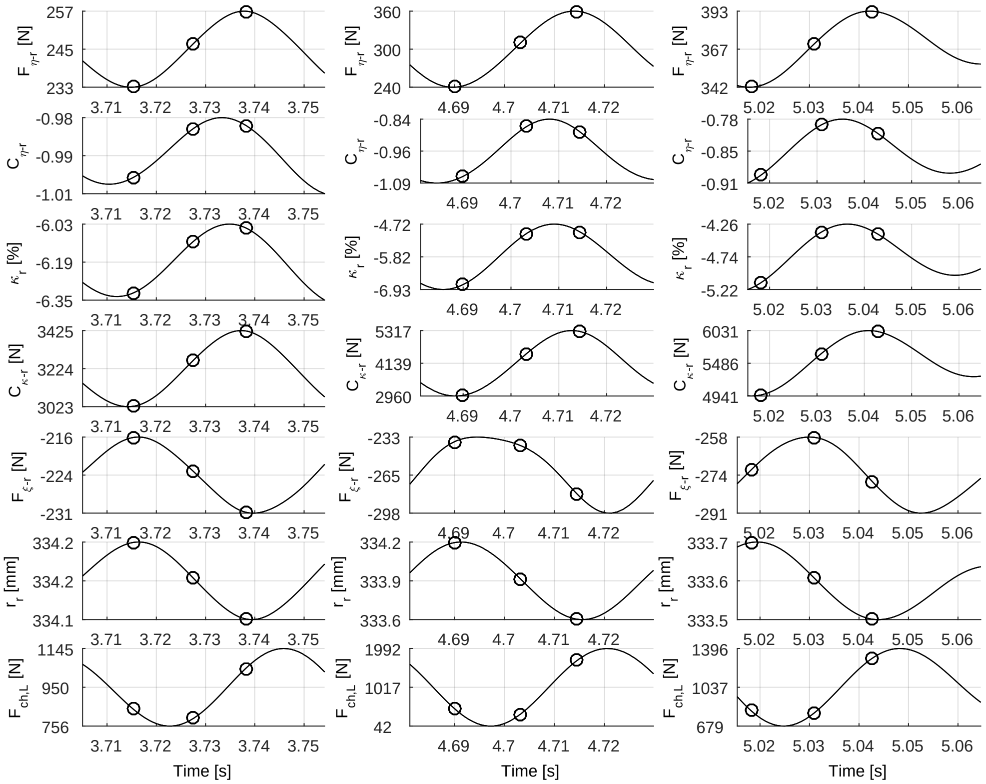

Figure 2.11: Phase lag among the oscillating variables.

Plotting the same oscillation quasi–periods in the $\kappa - F_\xi$ MF plane, different shapes can be observed in the resulting phase diagrams $F_\xi(\kappa)$, Figure 2.10 (right), where MF curves relative to minimum, maximum and mean vertical forces during each quasi–period are also displayed. Notice the dashed segments (in Figure 2.10, right) connecting the points of maximum and minimum slip for each quasi–period: they give a measure of the phase–lag between longitudinal ground force F_ξ and slip κ, from almost out–of–phase (increasing oscillation amplitude) towards almost in–phase (decreasing oscillation amplitude). In Figure 2.11 oscillations of each variable (rows) are displayed, taking the vertical force (first row) as a reference, and showing the evolution in the time domain (columns). The points in which the vertical force reaches its minimum, mean and maximum values are marked with a dot.

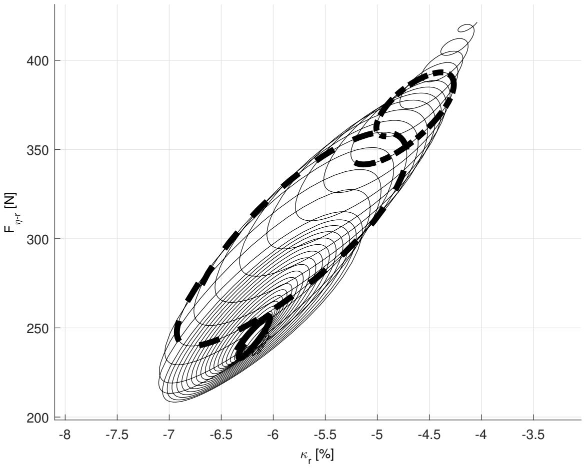

Figure 2.12: F_η - κ phase diagram for the rear tyre.

Phase–lags between rear slip κ and ground forces F_ξ and F_η can be noticed, also evidenced in the diagrams displayed in Figure 2.11. In particular, in the first column (increasing amplitude oscillations) κ and F_ξ are almost in counter–phase, while in the third column (decreasing amplitude oscillations) they are almost in–phase, as already observed in Figure 2.10 (left). Meanwhile, an increasing trend of C_κ (mean value) can be noticed, in parallel with a decreasing trend of C_η (absolute mean value). Therefore, increasing amplitude oscillations and decreasing ones are associated with different working points on the MF: higher C_κ values together with lower C_η values bring the system towards stability, and vice versa. Higher C_κ values are reached when reducing longitudinal slip, lower C_η values are reached when reducing load transfer, both effects due to reducing the braking effort. It can be deduced that the characteristic function of the tyre $F_{\xi 0}(\kappa_0, F_{\eta 0})$, and more precisely its partial derivatives (C_κ and C_η), play a major role in the self–excited mechanism under study.

The small variations of F_ξ are given by the first–order Taylor expansion already presented in Eq. 2.11 During the first, increasing amplitude, phase the system features large variations of C_κ, and this makes F_ξ more sensitive with respect to the second term of 2.11. When F_η is minimum, also C_κ is minimum, and the second term has a retarding effect on the increase of (absolute) F_ξ. This turns the shape of the F_ξ wave away from sinusoidal, resulting in a varying phase–lag with respect to all other quantities. In the last, decreasing amplitude, phase, the variations of C_κ are reduced, because the working point on the MF is now in the linear part of the curve, where C_κ is larger. The larger value of C_κ leads the model to stability. Therefore it can be stated that the parameters C_κ and C_η control the instability. In general, a higher C_κ or a lower (absolute) C_η can reduce the oscillations. On the contrary, an increase of (absolute) C_η represents a source of instability in the system. If C_η were null, F_η and F_ξ could be seen as independent quantities, the former varying mainly due to the load transfer, and the latter being dependent on the equilibrium equation of the wheel:

$$\ddot{\theta}_c(I_{yy-rr} + I_{yy-rw}) + (F_{ch-U} - F_{ch-L})r_{ws} - F_\xi r_r = 0 \tag{2.15}$$

If $C_\eta \neq 0$, a direct dependence of F_ξ on F_η is introduced and a fluctuation in vertical load affects also the rotation of the wheel, which, in turn, may produce further vertical load oscillations due to the coupling introduced by the chain transmission. Nevertheless, it must be noted that the self–excited instability must be given enough time to develop. This means that the rear tyre working points may cross the unstable region of the stability map (see Section 2.6) without showing oscillations in the time domain.

2.5 Frozen-time eigenvalue analysis

Eigenvalue analysis is a well established technique for predicting the stability. It requires to evaluate the response of a linearized model around an equilibrium configuration. In this conditions, the model exhibits asymptotically stable behaviour if and only if all the eigenvalues of the system have negative real part.

For motorcycles, eigenvalue analysis has been extensively applied even in non–equilibrium configurations (in this case referred to as frozen–time eigenvalue analysis) under the realistic hypothesis of slowly varying parameters [1]. In general, however, this hypothesis may be restrictive [33], and the bounds of validity of this technique have to be assessed [34].

Considering the linearization of the proposed model about the configuration assumed at t = 3.1 s (near maximum deceleration), stiffness and

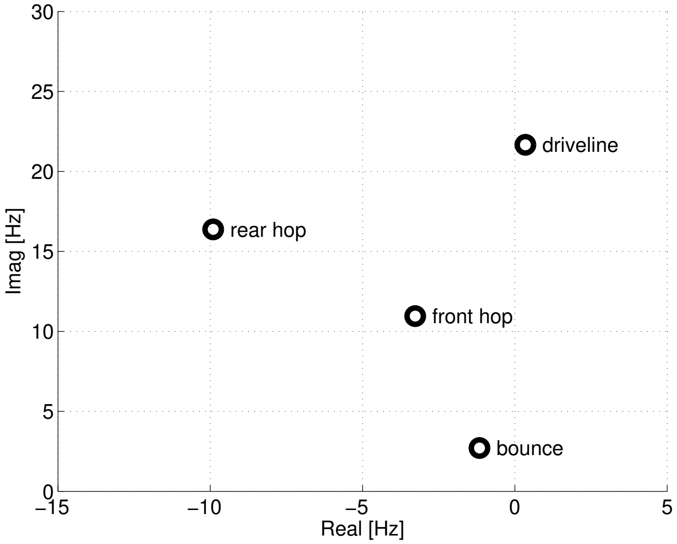

Figure 2.13: Root locus of the system at t = 3.1 s (frozen-time eigenvalues) in braking conditions.

damping matrices assume the following form:

$$\mathbf{K}(\mathbf{q}_0, \dot{\mathbf{q}}_0) = \left.\frac{\partial \mathbf{f}_j}{\partial \mathbf{q}_i}\right|_{\substack{\mathbf{q}=\mathbf{q}(3.1s)\\ \dot{\mathbf{q}}=\dot{\mathbf{q}}(3.1s)}} \qquad \mathbf{C}(\mathbf{q}_0, \dot{\mathbf{q}}_0) = \left.\frac{\partial \mathbf{f}_j}{\partial \dot{\mathbf{q}}_i}\right|_{\substack{\mathbf{q}=\mathbf{q}(3.1s)\\ \dot{\mathbf{q}}=\dot{\mathbf{q}}(3.1s)}} \tag{2.16}$$

It can be seen (Figure 2.13) that the real part of the driveline eigenvalue becomes positive (unstable). Consistently, the time domain simulation shows an instability at the frequency expressed by the driveline eigenvalue imaginary part (near 22 Hz).

Modal shapes of the system are shown in Figure 2.14, adopting the same normalization proposed for the constant velocity case at Section 2.2 (in clockwise order: bounce, front hop, rear hop and driveline modes). Main differences between the modal shapes for constant velocity and braking conditions can be summarized as follows:

- Front wheel rotation θ_a becomes the largest component in the bounce and front hop modes;
- In the rear hop mode, the main components α and r_r grow as well as the driveline components θ_c and θ_p;

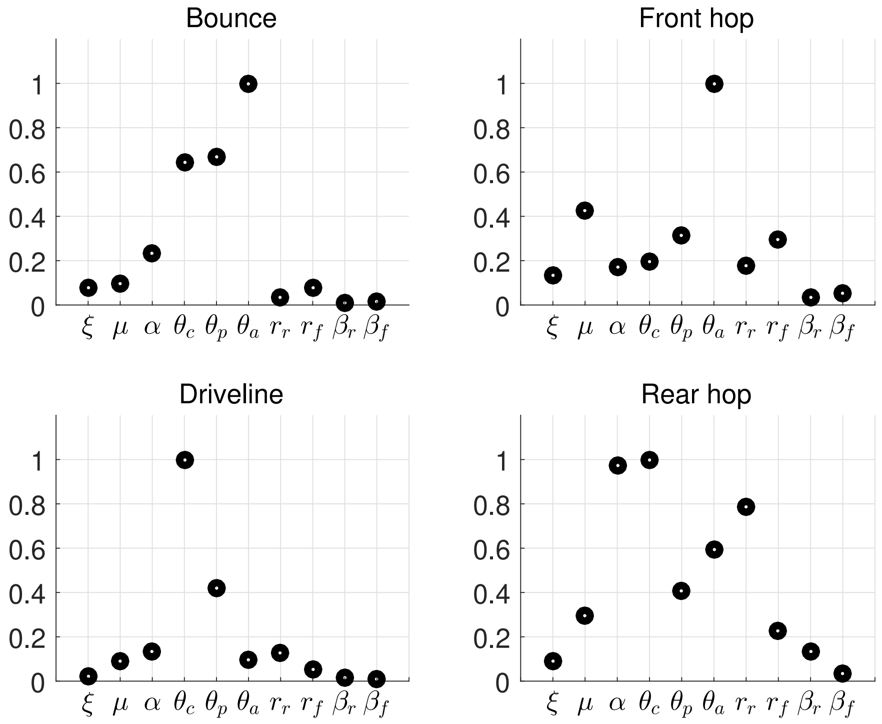

Figure 2.14: Modal shapes of the system in braking conditions.

- In the driveline mode, the components θ_c and θ_p grow, θ_c being the largest.

Again, it can be seen from time domain simulations (Figure 2.8) that the oscillating dofs during instability are mainly those related to the driveline and the rear suspension, according to the driveline modal shape.

Therefore, in this case, frozen–time eigenvalue analysis appears to be consistent with time domain results for the first part ($t \leq 3.1$ s) of the considered braking manoeuvre. In the general case however, for a time–variant system, frozen–time eigenvalues are not predictive of the stability. In fact, if the rate of change of the time–dependent parameters is sufficiently high, it is not possible to state that the system is asymptotically stable even if all the eigenvalues have negative real part [33].

During the considered braking unstable oscillation, the governing parameters change quickly as shown in Figure 2.9. The variation of the driveline eigenvalue for the three quasi–periods of Figure 2.10 is represented in Figure 2.15 (left). In the first, increasing amplitude phase, the real part of the driveline eigenvalue is always positive, while in the last, decreasing amplitude phase, it is always negative. However, in the central (maximum oscillation amplitude) phase, the eigenvalue real part oscillates around the stability threshold (imaginary axis). This uncertainty is addressed in the next section, where a time–invariant braking manoeuvre is analyzed.

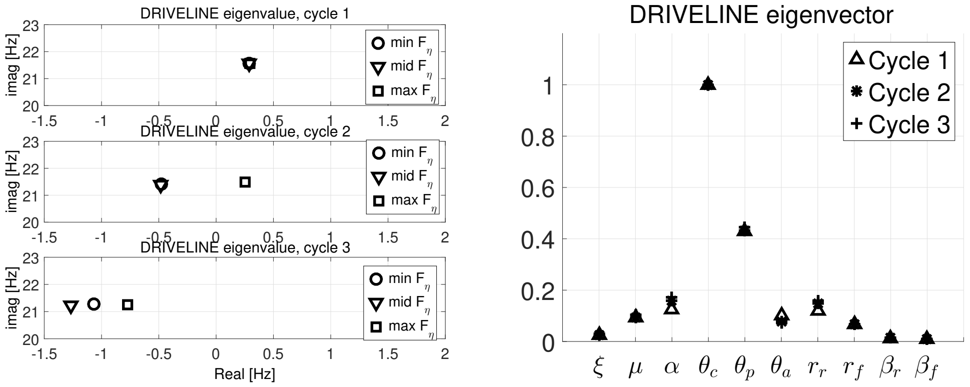

Figure 2.15: Driveline eigenvalue (left) and eigenvector (right) during the unstable phenomenon.

2.6 Stability threshold

In this section, a procedure to simulate a time–invariant braking manoeuvre is described, opening the possibility of drawing stability maps for the driveline mode by means of standard eigenvalue analysis. A time–invariant braking manoeuvre implies braking without changing neither the speed nor the configuration of the vehicle. Such stationary braking condition is simulated by imposing a longitudinal external acceleration generating a longitudinal forward force. In addition, an external torque is applied to the sprung mass, making it possible to properly simulate also the longitudinal load transfer. In this application the interest is focused on the values of C_κ and C_η the model is working with, i.e. on the working point on the rear tyre MF. Since any point in the MF region of interest can be reached varying the external actions, it is decided to drop the front brake input, so that the model brakes only by means of the engine.

The linearized equations of motion for the time–invariant system can be written in the form:

$$\mathbf{A}\dot{\mathbf{y}} + \mathbf{B}\mathbf{y} = \mathbf{0} \tag{2.17}$$

where, as opposed to Eq. 2.6, matrices $\mathbf{A}$ and $\mathbf{B}$ are now constant with respect to time. These matrices are known symbolically, and the descending left and right eigenproblems read:

$$\mathbf{z}_l^T(\lambda\mathbf{A} + \mathbf{B}) = \mathbf{0}; \quad (\lambda\mathbf{A} + \mathbf{B})\mathbf{z}_r = \mathbf{0} \tag{2.18}$$

where $\mathbf{z}_l$ and $\mathbf{z}_r$ are the left and right eigenvectors, and the superscript T stands for transpose of a vector.

The stability maps are drawn in the plane (C_κ,C_η), for fixed values of all the other parameters, due to the crucial role played by these two partial derivatives in controlling the stability of the driveline mode, as discussed in Section 2.4.

The dimension of the problem makes not advisable a direct application of the Routh–Hurwitz criterion [35]. Nevertheless, the stability maps of interest for the present study can be obtained recalling that a necessary and sufficient condition for stability is that all eigenvalues have negative real part. Hence, each point belonging to the stability threshold on the diagram (C_κ,C_η) can be found when the real part of the related diveline eigenvalue (say λ_{dl}) becomes zero.

As a consequence, it is necessary to asses an estimate of λ_{dl} as a function of C_κ and C_η, which can be achieved with an application of the Rayleigh quotient [36] in the following form:

$$\Lambda = Re(\lambda_{dl}) = -\frac{1}{2}\left(\frac{\mathbf{z}_l^T\mathbf{B}(C_\kappa, C_\eta)\mathbf{z}_r}{\mathbf{z}_l^T\mathbf{A}(C_\kappa, C_\eta)\mathbf{z}_r} + \frac{\mathbf{z}_l^{T*}\mathbf{B}(C_\kappa, C_\eta)\mathbf{z}_r^*}{\mathbf{z}_l^{T*}\mathbf{A}(C_\kappa, C_\eta)\mathbf{z}_r^*}\right) \tag{2.19}$$

where the superscript * stands for the complex conjugate of a vector.

Since the matrices $\mathbf{A}$ and $\mathbf{B}$ are known symbolically, solving $\Lambda(C_\eta) = 0$ for C_η yields a point on the stability threshold, which can be determined stepwise from a starting value, say ($C_{\kappa 0}$, $C_{\eta 0}$). The latter can be found by following a trial and error procedure from stationary braking manoeuvres with proper values of external accelerations and load transfers.

The n-th point (say, ($C_{\kappa n}$,$C_{\eta n}$)) of the stability threshold is obtained as follows. $C_{\kappa n}$ is increased of a fixed quantity ΔC_κ ($C_{\kappa n} = C_{\kappa n-1} + \Delta C_\kappa$); the corresponding value of $C_{\eta n}$ on the stability threshold is the one for which the real part of the driveline eigenvalue becomes zero. At each iteration the real part of the eigenvalue is approximated by:

$$\Lambda \cong -\frac{1}{2}\left(\frac{\mathbf{z}_{ln-1}^T\mathbf{B}(C_{\kappa n}, C_\eta)\mathbf{z}_{rn-1}}{\mathbf{z}_{ln-1}^T\mathbf{A}(C_{\kappa n}, C_\eta)\mathbf{z}_{rn-1}} + \frac{\mathbf{z}_{ln-1}^{T*}\mathbf{B}(C_{\kappa n}, C_\eta)\mathbf{z}_{rn-1}^*}{\mathbf{z}_{ln-1}^{T*}\mathbf{A}(C_{\kappa n}, C_\eta)\mathbf{z}_{rn-1}^*}\right) \tag{2.20}$$

where $\mathbf{z}_{ln-1}$ and $\mathbf{z}_{rn-1}$ are the left and right driveline eigenvectors computed at the previous step ($n-1$), $\mathbf{A}$ and $\mathbf{B}$ are the system matrices evaluated at the current $C_{\kappa n}$ as a function of C_η. A zero–find routine solves $\Lambda(C_\eta) = 0$ for C_η, and the resulting value is assigned to $C_{\eta n}$. The matrices $\mathbf{A}$ and $\mathbf{B}$ obtained from $C_{\kappa n}$ and $C_{\eta n}$ define the new current left and right eigenproblems, yelding the new eigenvectors $\mathbf{z}_{ln}$ and $\mathbf{z}_{rn}$, and the next step begins.

A schematic of the algorithm therefore reads:

```
1: Trial and error calculation of the first point of the stability margin:
   $C_{\kappa n-1} = C_{\kappa 0}$, $C_{\eta n-1} = C_{\eta 0}$, $n = 1$;

2: Solution of:
   $\mathbf{z}_{l0}^T(\lambda\mathbf{A} + \mathbf{B}) = \mathbf{0}$ and $(\lambda\mathbf{A} + \mathbf{B})\mathbf{z}_{r0} = \mathbf{0}$
   with
   $\mathbf{A} = \mathbf{A}(C_{\kappa n-1}, C_{\eta n-1})$ and $\mathbf{B} = \mathbf{B}(C_{\kappa n-1}, C_{\eta n-1})$
   yielding
   $\mathbf{z}_{ln-1}$, $\mathbf{z}_{rn-1}$
```

```
3: Reset matrices:
   $\mathbf{A} = \mathbf{A}(C_{\kappa n-1} + \Delta C_\kappa, C_\eta)$,
   $\mathbf{B} = \mathbf{B}(C_{\kappa n-1} + \Delta C_\kappa, C_\eta)$

4: Solution of:
   $\frac{\mathbf{z}^T_{ln-1}\mathbf{B}(C_{\kappa n}, C_\eta)\mathbf{z}_{rn-1}}{\mathbf{z}^T_{ln-1}\mathbf{A}(C_{\kappa n}, C_\eta)\mathbf{z}_{rn-1}} + \frac{\mathbf{z}^{T*}_{ln-1}\mathbf{B}(C_{\kappa n}, C_\eta)\mathbf{z}^*_{rn-1}}{\mathbf{z}^{T*}_{ln-1}\mathbf{A}(C_{\kappa n}, C_\eta)\mathbf{z}^*_{rn-1}} = 0$
   yielding
   $C_{\eta n}$

5: Reset matrices:
   $\mathbf{A} = \mathbf{A}(C_{\kappa n}, C_{\eta n})$,
   $\mathbf{B} = \mathbf{B}(C_{\kappa n}, C_{\eta n})$
```

Then repeat steps 2 to 5 for $n = 2, ..., N$.

For assessment of the results of the proposed algorithm, the same stability threshold is evaluated numerically with a completely different procedure for a number of (C_κ,C_η) couples obtained from time domain simulations. Each stationary–braking manoeuvre is defined by a selected couple of values of longitudinal acceleration and load transfer. A higher acceleration requires a higher value of longitudinal force F_ξ in order to keep constant the velocity, therefore the rear slip increases while C_κ decreases. At the same time, a variation of load transfer ΔF_η modifies the vertical load on the rear tyre, thus changing C_η. The combination of longitudinal and vertical forces defines the working point of each manoeuvre on the rear tyre MF and, consequently, the values of C_κ and C_η. The possibility of controlling independently C_κ and C_η through external fictitious actions allows to explore the model behaviour for the entire range of interest of the two governing parameters. At the end of each time domain simulation, if the driveline eigenvalue has negative real part, the working point of the rear tyre is considered stable (marked with a star in Figure 2.16). If the driveline eigenvalue has positive real part, the working point is considered unstable (marked with a square in Figure 2.16).

Figure 2.16 shows a comparison between the results obtained with the two proposed methods. As expected from time domain simulations (Section

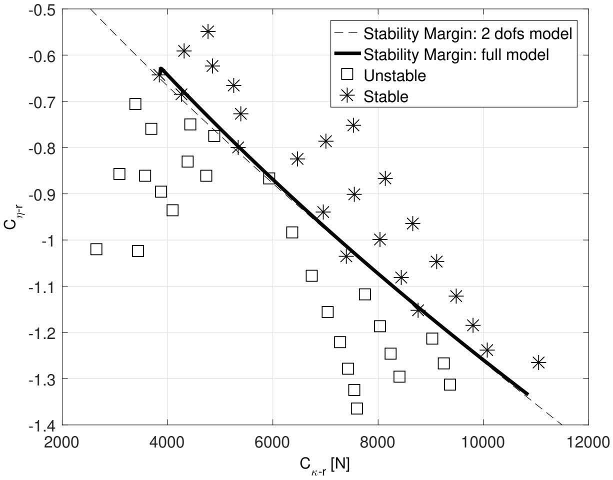

Figure 2.16: Stability threshold for v = 100 km/h (solid line) compared to time domain stable/unstable couples (C_κ, C_η). The dashed line refers to the simplified 2 dofs model exposed in [5]. See Section 2.7 for details.

2.4), the stable region is the part of the plane with high values of C_κ and low (absolute) values of C_η.

It should also be noticed that, while each stationary manoeuvre is represented by a single point on the $C_\kappa - C_\eta$ diagram, transient braking manoeuvres would be represented by time–dependent trajectories. Drawing such a trajectory for the manoeuvre described in the previous sections clarifies the relation between the stability of the time–dependent model and the stability threshold obtained in steady–state conditions. In Figure 2.17 two different stability thresholds are drawn, the first (solid line) for $v = 138$ km/h, the second (dotted line) for $v = 80$ km/h. These are the velocities at which, in the transient manoeuvre, the stability takes places and vanishes. After the application of engine brake, the trajectory of the transient manoeuvre moves towards the bottom–left part of the diagram (low C_κ, high $|C_\eta|$), well inside the unstable region bounded by the first threshold. With a minimal time delay, the instability shows up as quasi–cycles of increasing amplitude. As the velocity decreases, and the average vertical load on the rear tyre increases, the quasi–cycles center slowly moves back to the upper–right part of the diagram, crossing the second threshold at v = 80 km/h. From this

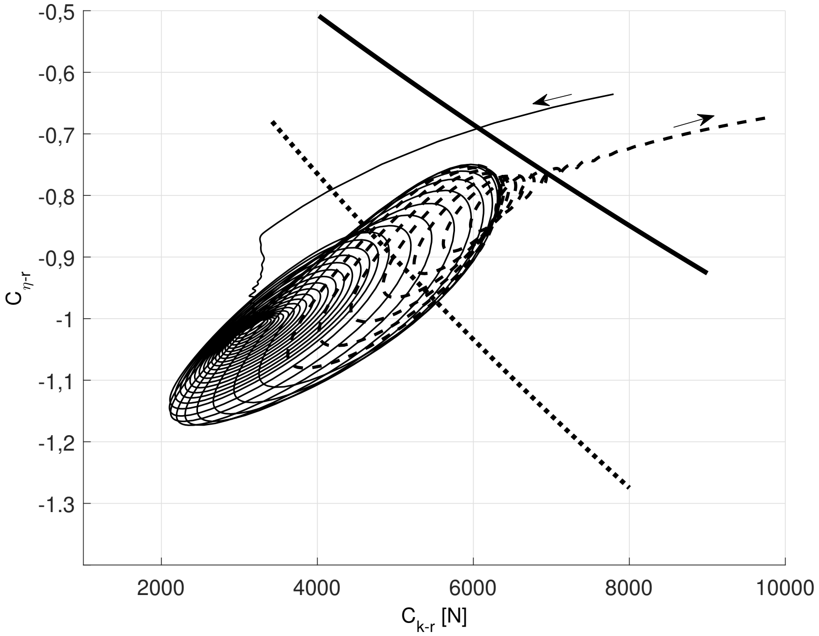

Figure 2.17: Stability thresholds for v = 138 km/h (solid line) and v = 80 km/h (dotted line) compared with transient manoeuvre trajectory (2.5 s $< t <$ 6 s).

moment on (highlighted by changing the line style from solid to dashed), the quasi–cycles amplitude starts to decrease, and the instability eventually vanishes.

2.7 Comparison with a simplified model

The results of the analysis carried out with the multibody motorcycle model are compared with those of the simplified linearized model proposed by Sorrentino and Leonelli [5]. The geometry of this model is displayed in Figure 2.18. This is a rear motorcycle suspension model with 2–dofs (wheel rotation ϑ and vertical displacement z), travelling at constant imposed speed V_0 under the action of chain transmission force F_c and tyre ground forces (F_ξ and F_η); here, the ground forces names have been changed in order to match the nomenclature of the present work.

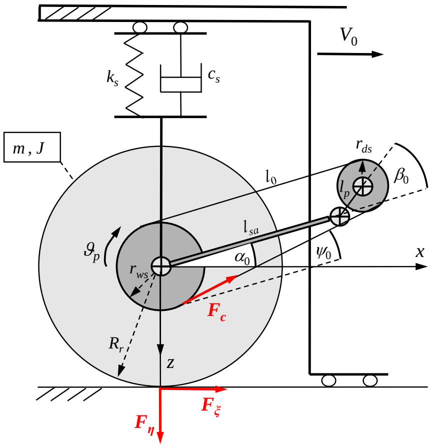

Figure 2.18: Geometry of the simplified 2–dofs model of a motorcycle rear assembly employed in [5]

2.7.1 Simplified model parameters

In order to allow a consistent comparison between the full and the simplified model, a preliminary work of parameter tuning was necessary. The primary focus of the tuning process was on the natural frequency of the mode at the stability threshold, since the target was to quantitatively compare the two models in terms of stability maps (C_κ–C_η plane). Thus, the attention was given to getting comparable natural frequencies between the full and the simplified model.

To this purpose, the inertial and damping properties of the 2–dofs model were modified from their value in [5]. The equivalent translating unsprung mass m:

$$m = \frac{m_0 l_{sa}^2 + J_{sa}}{l_{sa}^2 \cos^2 \alpha_0} \tag{2.21}$$

and the wheel moment of inertia J have been reduced, taking into account that the 2–dofs model features infinite sprung mass as well as infinite powertrain inertia. Due to mass modification, also the damping coefficient c_s

has been proportionally reduced. The adopted criterion has been keeping constant the factor:

$$\zeta_s = \frac{c_s}{2\sqrt{mk}} \tag{2.22}$$

where $k = k_s + k_z$. With parameters in Tab. 2.2, at the stability threshold the eigenvalues of the 2–dofs model are about:

- Real 0.0 Hz, Imaginary 22.0 Hz
- Real −7.0 Hz, Imaginary 21.0 Hz

A comprehensive list of all the 2–dofs model parameters values is reported in Table 2.2. For the sake of clarity, the name of some parameters have been changed in order to match the nomenclature of the present work.

2.7.2 Comparison between the two models

The full and the simplified models present relevant differences; nevertheless the resulting unstable behaviours appear to be closely related. In fact, in both cases, a self–excited vibration is detected when strong engine brake torque is applied, due to a mode which becomes unstable in the frequency range of motorcycle chatter, consisting of an angular oscillation of the driveline coupled with a rear wheel bounce.

It was demonstrated [5] that for the 2–dofs model the key role in the switching mechanism to driveline instability is played by the nonlinear characteristic slip function of the tyre $F_{\xi 0}(\kappa_0, F_{\eta 0})$, and more precisely by its partial derivatives with respect to the stationary components of the vertical ground force (C_η) and longitudinal slip (C_κ). The energy balance evaluation over one period of oscillation showed that the stability threshold is reached for a certain value of the phase–lag (say, ϕ) between the non–stationary components of the slip κ and longitudinal ground force F_ξ. It was also found that C_κ and C_η can increase ϕ above the critical value, giving rise to a non–conservative restoring force. In these conditions the suspension damper c_s is not able to dissipate the energy supplied by the longitudinal ground force F_ξ, thus leading the system to instability.

The results of the analysis carried out with the multibody model, in particular at Sections 2.4 (Figure 2.11) and 2.6 (Figure 2.16), show full consistency with those of the simplified 2–dofs model. As in the simplified model, the phase–lag between κ and F_ξ has a crucial role in the evolution of the

Table 2.2: Parameters adopted in the simplified 2–dofs linear model. In parenthesis: nomenclature as in Sorrentino and Leonelli [5]. Values adopted in the multibody model. Arrows indicate modified values.

Pinion radius	$r_{ds}(r_p) = 0.040$ m
Wheel sprocket radius	$r_{ws}(r_c) = 0.100$ m
Swingarm length	$l_{sa} = 0.590$ m
Rear wheel unloaded radius	$R_r(r) = 0.320$ m
Axle distance	$l_p = 0.080$ m
Swingarm angle (stationary)	$\alpha_0 = 0.16$ rad
Angle between swingarm and l_p	$\beta_0 = 0.12$ rad
Rear wheel mass	$m_0 = 14.5$ kg
Swingarm inertia moment (pivot)	$J_{sa} = 1.46$ kgm^2
Equivalent unsprung mass	$m = 18.3$ kg $\rightarrow m = 15$ kg
Rear wheel moment of inertia	$J = 0.83$ kgm^2 $\rightarrow J = 0.56$ kgm^2
Suspension ground damping	$c_s = 1040$ Ns/m $\rightarrow c_s = 940$ Ns/m
Suspension ground stiffness	$k_s = 4.45 \cdot 10^4$ N/m
Tyre radial stiffness	$k_z = 1.7 \cdot 10^5$ N/m
Chain stiffness	$k_{ch}(k_c) = 1.15 \cdot 10^6$ N/m
Longitudinal slip (stationary)	$\kappa_0 = -0.04$
Rear longitudinal force (stationary)	$F_{\xi 0}(F_{x0}) = -200$ N
Rear slip stiffness (stationary)	$C_{\kappa 0} = 4000$ N
Partial derivative of $F_{\xi 0}(F_{x0})$ w.r.t. $F_{\eta 0} F_{z0}$	$C_{\eta 0}(-\chi) =$ -0.65

identified unstable phenomenon, and it is primarily controlled by the characteristic slip function of the tyre, and in particular by C_η and C_κ.

The two models can be quantitatively compared in a $C_\kappa - C_\eta$ diagram in terms of stability maps, which for the 2–dofs model were analytically determined via Routh–Hurwitz criterion [35]. The initializing parameters for the 2–dofs model are reported in Table 2.2, with the same numerical values adopted for the multibody model, except for the inertial and damping properties, as explained in the previous section.

With the adopted parameters, the 2–dofs model becomes unstable at about 22 Hz. The resulting stability map is superimposed on the $C_\kappa - C_\eta$ diagram of Figure 2.16, almost overlapping the threshold given by the stationary–braking multibody model. Phase diagrams $F_\xi(\kappa)$ of the two models at the limit of stability are displayed and compared in Figure 2.19. The values of C_κ and C_η for the full multibody model have been chosen in order to obtain oscillation amplitude comparable to that of the 2–dofs model.

As an example, in Figure 2.19 a phase diagram $F_\xi(\kappa)$ in the $\kappa - F_\xi$ plane obtained with the 2–dofs model (top) is compared to the corresponding one computed during a transient braking manoeuvre (bottom): at the stability limit, the latter develops self–excited oscillations comparable in amplitude with those of the stationary model at a point (C_κ, C_η) well into the unstable region of the map, Figure 2.16. The diagrams in Figure 2.19 also show that at the selected stability limit, the phase–lags between κ and F_ξ given by the two models are about the same.

It can be concluded that the relevant features and parameters controlling the onset and development of driveline chatter instability are those included in the 2–dofs model, all the remaining features and parameters of the multibody model playing a secondary role.

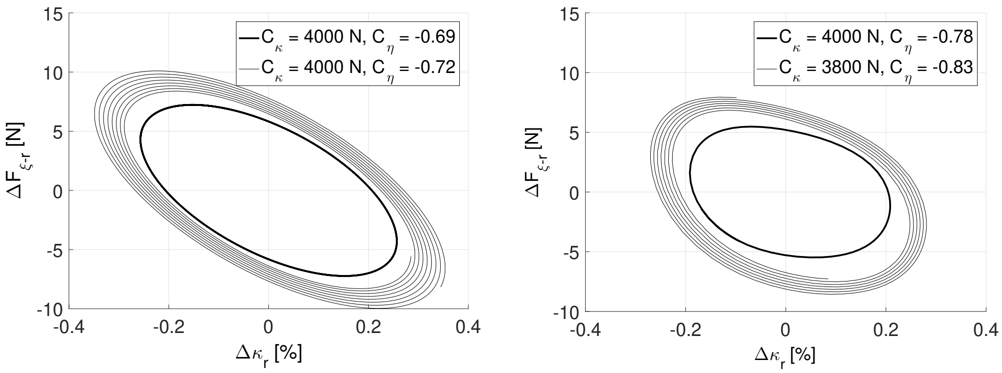

Figure 2.19: Unstable cycles for the simplified 2 dofs model (left) and the full model (right). Here the longitudinal force $F_{\xi-r}$ and slip κ_r are displayed as a Δ w.r.t. the equilibrium configuration value.

Chapter 3

Front wheel patter instability

Introduction

Affecting especially performances of road racing motorcycles, locking of the front wheel before reaching the maximum longitudinal ground force is a problem that can arise during heavy braking in straight motion. It shows up as a sudden deceleration of the front wheel, since in these conditions the longitudinal ground force is not able to balance the applied braking force. As revealed by data analysis on instrumented motorcycles, this extreme circumstance is preceded by vibrations in a frequency range between 7 and 10 Hz, involving fluctuations of both spin velocity of the front wheel and pitch of the vehicle, which cause oscillations of the front downforce at the same frequency.

This phenomenon, referred to as front wheel patter, was first studied by Sharp and Giles [3] on the basis of previous work on automobile axle tramping vibrations [29], leading to the definition of a four degrees of freedom minimal model. In [3] only the front assembly was considered, pivotting about a horizontal axis and spring restrained to an infinitely massive rear frame, with additional allowed motions consisting of plunging of telescopic forks, spinning of the wheel and spinning of the tyre tread band, restrained by the tyre carcass elasticity. Stability was investigated by imposing constant travelling speed to the rear frame, then integrating numerically the non–linear constant–coefficient equations of motion in the time domain.

With realistic choices of parameter values, self–excited oscillations were identified close to the natural frequency of the wheel–hop mode, however with a substantial component of motion given by the forks pivoting on the rear frame compliance, resulting in an elliptical orbit of the wheel spindle. High values of tyre load during backward motion of the wheel were detected, together with low values during forward motion, providing the supply of energy to vibration from the forward motion of the vehicle as a whole.

As a result, it was found that stability is significantly enhanced by reducing the vehicle speed, by reducing the frictional coupling between tyre and ground, by increasing the damping amounts and by mismatching the frame compliance by the equivalent vertical stiffness of the front assembly (or, in other words, avoiding close matching of the natural frequency of the forks pivoting on the frame compliance with the natural frequency of vertical motion of the wheel on the tyre and suspension springs). On the contrary, the tyre carcass (torsional) flexibility turned out to play a negligible role, giving a very small stabilizing contribution. Reference [3] created a basis for further investigations on unstable oscillations leading to front wheel locking, but, to the best of the author's knowledge, no other published study has dealt with it ever since.

The aim of this study is to extend the analysis developed in [3] to clearly identify the actual switching mechanism to instability and its governing parameters, with additional highlights on analogies and differences with respect to chatter oscillations, as investigated in [5]. First, a modified minimal model of the front assembly is proposed, with centre of rotation of the upper forks positioned out of the fork line, for simulating also modes involving pitching of the motorcycle's main frame (not considered in [3]); its equations of motion are derived in non–linear form and then linearized with respect to equilibrium–states, by imposing stationary values of forward speed during braking; the proposed model is then studied in terms of modal analysis and stability maps. Second, the results are compared to numerical simulations obtained from a full motorcycle multibody model, as described in Appendix A. This analysis is restricted to planar motion, considering running straight ahead braking manoeuvres not including lateral dynamics. It should at least be mentioned that, during cornering manoeuvres, out–of–plane modes would come into play (due to anti–symmetrical or lateral dynamics), causing possible merging effects with in–plane modes: as detected by Koenen [30], at high roll angles a mode involving front–hop and wobble components (also referred to as front wheel patter, but substantially different from the one herein studied) may become unstable even in case of free rolling conditions. Such interactions with lateral components at high roll angles are expected to be further modified when considering braking forces, representing a research subject left open to future investigations.

3.1 Minimal model

A planar minimal model of a motorcycle is considered, with three degrees of freedom. The equations of motion are derived in non–linear form and then linearized with respect to an equilibrium–state, by imposing a stationary value of forward speed during braking. A linearized expression of the longitudinal ground force with respect to the same equilibrium–state is also provided, as a function of the state variables, playing a fundamental role in stability analysis.

3.1.1 Description of the model

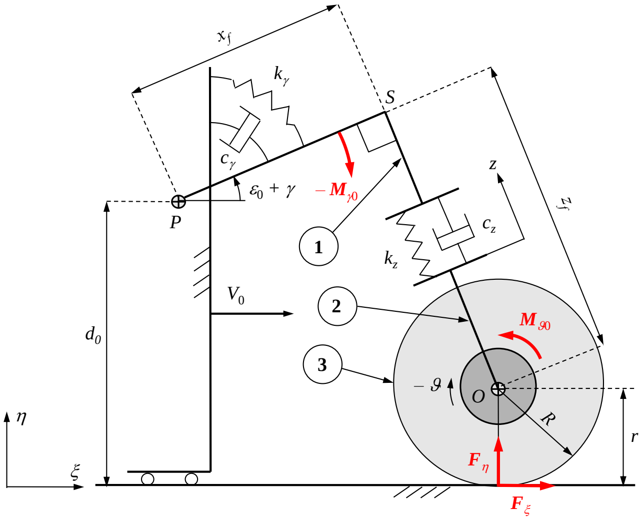

Figure 3.1: Schematic of the proposed minimal model

The model consists of three rigid bodies as represented in Figure 3.1: the main frame rigidly connected to the upper steering assembly (1), the lower steering assembly (2) and the front wheel assembly (3).

Body 1 can pivot with an angle γ (positive if counterclockwise in Figure 3.1) around a point P (fictitious, since such a fixed point in a motorcycle clearly does not exist) connected to a rigid frame translating at imposed constant speed V_0 in forward direction ξ. Its centre of gravity is positioned in P, with moment of inertia J_1 about P, and it is restrained to the rigid translating frame by a torsion spring of stiffness k_γ parallel to a torsional viscous damper of constant c_γ (not displayed in Figure 3.1). The upper and lower steering assemblies, connected to each other by telescopic forks, are restrained by a suspension spring of stiffness k_z, parallel to a viscous damper of constant c_z, while their relative sliding is described by a coordinate z, as represented in Figure 3.1. The lower steering assembly 2 is connected to the front wheel assembly 3 by a revolute joint in point O (rim centre), assuming zero fork offset. Bodies 2 and 3 together have total mass m; the centre of gravity of body 2 is assumed to be positioned in O (with moment of inertia J_2), as the one of body 3 (with moment of inertia J_3). The wheel rolls on a perfectly flat surface, with angular displacement ϑ (positive if counterclockwise in Figure 3.1), unloaded radius R, loaded radius r and radial stiffness k_r.

The model has three degrees of freedom, represented by the lagrangian coordinates γ, z and ϑ. The actual distance between O and P is given by a pair of parameters, say x_f (orthogonal to the actual fork line) and z_f (dependent on z, parallel to the actual fork line), as shown in Figure 3.1.

An equilibrium–state (identified by a subscript 0) is considered at constant travelling speed V_0, under the effects of a constant braking torque $M_{\vartheta 0} > 0$ applied to body 3, and of a constant pitching moment $M_{\gamma 0} < 0$ applied to body 1 (simulating a longitudinal load transfer due to braking). These actions produce a ground reaction on the wheel (with longitudinal component $F_{\xi 0}$ and vertical component $F_{\eta 0} - mg$), along with a rotation $\gamma_0 < 0$ of body 1 (yielding a caster angle ε_0 in the equilibrium–state), a compression $z_0 > 0$ of the suspension spring and a compression $h_0 > 0$ of the tyre (with $k_\gamma \gamma_0$, $k_z z_0$ and $k_r h_0$ playing the role of spring preloads).

Adopting the following compact notation:

$$\begin{cases} \hat{s} & = \sin(\varepsilon_0 + \gamma) \\ \hat{c} & = \cos(\varepsilon_0 + \gamma) \end{cases} , \begin{cases} \hat{s}_0 & = \sin(\varepsilon_0) \\ \hat{c}_0 & = \cos(\varepsilon_0) \end{cases} \tag{3.1}$$

the actual (ξ_t, η_t) and equilibrium–state (ξ_0, η_0) distances between points O and P in the ξ and η directions can be written as:

$$\begin{cases} \xi_t &= \xi_O - \xi_P &= x_f \hat{c} + z_f \hat{s} \\ \eta_t &= \eta_P - \eta_O &= -x_f \hat{s} + z_f \hat{c} \end{cases} , \begin{cases} \xi_0 &= \xi_{O0} - \xi_{P0} &= x_f \hat{c}_0 + z_{f0} \hat{s}_0 \\ \eta_0 &= \eta_{P0} - \eta_{O0} &= -x_f \hat{s}_0 + z_{f0} \hat{c}_0 \end{cases} \tag{3.2}$$

where:

$$\begin{cases} z_f &= l - (z_0 + z) \\ z_{f0} &= l - z_0 \end{cases} \tag{3.3}$$

and l is the distance between O and S in the unloaded case. During a small perturbation of the equilibrium–state, the actual radius r of the loaded wheel depends on the actual compression h of the tyre, which in turn is a function of coordinates γ and z:

$$r = R - (h_0 + h) \quad , \quad r_0 = R - h_0 \quad , \quad h = \eta_t - \eta_0 \tag{3.4}$$

Consequently, the actual vertical ground force F_η can be expressed as:

$$F_\eta = k_r (h_0 + h) \tag{3.5}$$

A full list of parameters describing the proposed model is reported in Appendix B.2. It presents two differences with respect to the model studied in [3]: first, the centre of rotation of the upper forks P can be positioned out of the fork line, for simulating also modes involving pitching of the motorcycle's main frame; second, the wheel assembly is considered as a single body, since in [3] the torsional compliance of the tyre was recognized to play a negligible role in the development of instability, which was confirmed by simulations performed with the multibody model herein adopted, considering rigid–ring tyres.

3.1.2 Non–linear equations of motion

The equations of motion are derived via Lagrange equations, including in the generalized forces the braking torque $M_{\vartheta 0}$ and both the components F_ξ and F_η of the ground reaction, but not the pitching moment M_γ, accounted for in the dissipation function and in the potential energy. Then the system's kinetic energy T, dissipation function D and potential energy U read:

$$\begin{aligned}
T &= \frac{1}{2}\left\{m\left[(x_f\dot{\gamma}+\dot{z})^2+(z_f\dot{\gamma})^2\right]+J_{12}\dot{\gamma}^2+J_3\dot{\vartheta}^2\right\}\\
D &= \frac{1}{2}\left(c_\gamma\dot{\gamma}^2+c_z\dot{z}^2\right)\\
U &= \frac{1}{2}\left\{k_\gamma\left[(\gamma+\gamma_0)^2-\gamma_0^2\right]+k_z\left[(z+z_0)^2-z_0^2\right]\right\}-mgh
\end{aligned} \tag{3.6}$$

where $J_{12} = J_1 + J_2$, yielding the three equations of motion in the form:

$$\begin{cases}
m\left[\left(x_f^2+z_f^2\right)\ddot{\gamma}+x_f\ddot{z}-2z_f\dot{\gamma}\dot{z}\right]+J_{12}\ddot{\gamma}+c_\gamma\dot{\gamma}+k_\gamma(\gamma+\gamma_0)+mg\xi_t=Q_\gamma\\
m\left[x_f\ddot{\gamma}+\ddot{z}+z_f\dot{\gamma}^2\right]+c_z\dot{z}+k_z(z+z_0)+mg\hat{c}=Q_z\\
J_3\ddot{\vartheta}=Q_\vartheta
\end{cases} \tag{3.7}$$

with generalized forces:

$$\begin{cases}
Q_\gamma = F_\xi\eta_t+F_\eta\xi_t-M_{\vartheta 0}\\
Q_z = -F_\xi\hat{s}+F_\eta\hat{c}\\
Q_\vartheta = rF_\xi+M_{\vartheta 0}
\end{cases} \tag{3.8}$$

in which, recalling Eqs. 3.1–3.5, explicit relations for ξ_t, η_t, r and F_η can be introduced in terms of coordinates γ and z.

3.1.3 Linearized constitutive equation of the longitudinal ground force

The linearized constitutive equation of the longitudinal ground force F_ξ is derived by considering the definition of longitudinal slip coefficient κ and its equilibrium–state expression κ_0:

$$\kappa = -\frac{V_S}{V} \Rightarrow \kappa_0 = -\left(1+\frac{\rho_0\omega_0}{V_0}\right) \tag{3.9}$$

where V is the actual translating speed of the wheel spindle (point O, in Figure 3.1), V_S is the actual slip velocity, $\omega_0 < 0$ is the equilibrium–state angular speed of the rim and ρ_0 is the equilibrium–state free rolling radius of the wheel, evaluated at $\kappa_0 = 0$ (during braking, if $V > 0$ then $\kappa < 0$). Given ω_0 and V_0, the effective rolling radius ρ_{κ_0} (evaluated at $\kappa \neq 0$) is:

$$\rho_{\kappa 0} = -\frac{V_0}{\omega_0} \Rightarrow \frac{\rho_0}{\rho_{\kappa 0}} = 1 + \kappa_0 \tag{3.10}$$

Hence in the case of small oscillations with respect to an equilibrium–state, κ takes the form:

$$\kappa = -\left(1 + \frac{\rho\omega}{V}\right) \Leftrightarrow \kappa_0 + \tilde{\kappa} = -\left[1 + \frac{(\rho_0 + \tilde{\rho})(\omega_0 + \tilde{\omega})}{V_0 + \tilde{V}}\right] \tag{3.11}$$

where ρ is the actual free rolling radius and the tilde symbol denotes the non–stationary components of κ, ρ, ω and V. The last two of them can be approximated by:

$$\begin{aligned} \tilde{\omega} &\simeq \dot{\vartheta} \\ \tilde{V} &\simeq \eta_0 \dot{\gamma} - \hat{s}_0 \dot{z} \end{aligned} \tag{3.12}$$

In the first of Eqs. 3.12, only the non–stationary component of the rim angular speed has been considered, disregarding the torsional rate of deformation of the tyre [37], or equivalently assuming a relaxation length so small to be negligible [5, 6]. The non–stationary component of the free rolling radius ρ can be expressed as a function of the tyre compression h by means of a dimensionless parameter e, accounting for the vertical position of the centre of rotation below the ground level:

$$\tilde{\rho} = -(1-e)h \quad \text{with} \quad 0 \leq e \leq 1 \quad , \quad h \simeq -\left(\xi_0\gamma + \hat{c}_0 z\right) \tag{3.13}$$

which means that the free rolling radius changes with tyre deflection at a rate given by the factor $(1-e)$ [37]. Taking into account Eqs. 3.10–3.13, the non–stationary component of κ can then be linearized with respect to ρ, ω and V:

$$\begin{aligned} \tilde{\kappa} &= \left.\frac{\partial \kappa}{\partial \rho}\right|_0 \tilde{\rho} + \left.\frac{\partial \kappa}{\partial \omega}\right|_0 \tilde{\omega} + \left.\frac{\partial \kappa}{\partial V}\right|_0 \tilde{V} \\ &= \frac{1}{V_0}\left\{-\rho_0\dot{\vartheta} + (1+\kappa_0)\left[(1-e)\frac{V_0}{\rho_0}\left(\xi_0\gamma + \hat{c}_0 z\right) - \eta_0\dot{\gamma} + \hat{s}_0\dot{z}\right]\right\} \end{aligned} \tag{3.14}$$

The linearized non–stationary component of F_ξ can now be defined as a function of both $\tilde{\kappa}$ and the non–stationary component of the vertical ground force F_η:

$$\begin{gathered}\tilde{F}_\xi = C_\kappa \tilde{\kappa} + C_\eta \tilde{F}_\eta \\ \text{with} \\ C_\kappa = \left(\frac{\partial F_{\xi 0}}{\partial \kappa_0}\right)_{F_\eta = F_{\eta 0}}, C_\eta = \left(\frac{\partial F_{\xi 0}}{\partial F_{\eta 0}}\right)_{\kappa = \kappa_0}, \tilde{F}_\eta \simeq -k_r \left(\xi_0 \gamma + \hat{c}_0 z\right)\end{gathered} \tag{3.15}$$

where $C_\kappa > 0$ denotes the stationary slip stiffness of the tyre evaluated at a longitudinal slip κ_0 under the vertical force $F_{\eta 0}$, while $C_\eta < 0$ expresses the local dependency of $F_{\xi 0}$ with respect to $F_{\eta 0}$. Even though C_κ and C_η in Eq. 3.15 appear to be mathematically independent, in fact they are related to the stationary equilibrium point on the nonlinear characteristic slip function of the tyre $F_{\xi 0}$ (κ_0, $F_{\eta 0}$), usually described by MFs, Magic Formulas [32]. Introducing Eq. 3.14 in Eq. 3.15, and approximating the free rolling radius ρ_0 with the outer radius of the unloaded wheel R, yields:

$$\begin{gathered}\tilde{F}_\xi = A \left[-R\dot{\vartheta} + (1+\kappa_0)\left(-\eta\dot{\gamma} + \hat{s}_0 \dot{z}\right)\right] + B\left(\xi_0 \gamma + \hat{c}_0 z\right) \\ \text{with} \\ A = \frac{C_\kappa}{V_0}, \quad B = \frac{C_\kappa}{R}(1+\kappa_0)(1-e) - C_\eta k_r\end{gathered} \tag{3.16}$$

where A is a damping parameter [Nsm^{-1}] and B a stiffness parameter [Nm^{-1}], which highlight the dependency of F_ξ with respect to the state variables.

3.1.4 Linearized equations of motion

The system's equilibrium configuration at $V = V_0$ is determined after setting the external actions and the independent parameters characterizing the model, i.e. four geometric parameters (R, l, x_f, ε_0), along with three stiffness parameters (k_γ, k_z, k_r) and the mass parameter (m).

Notice that R and m are the only parameters actually independent from the equilibrium configuration, since the position of point P, assumed known, changes according to the equilibrium state as well as the stiffness parameters, due to non–linear behaviour.

For the sake of convenience, the external actions are expressed in terms of ground force components ($F_{\xi 0}$, $F_{\eta 0}$) instead of braking and pitching moments

$(M_{\vartheta 0},\ M_{\gamma 0})$. Hence, recalling the definitions of $\hat{c}_0$ and $\hat{s}_0$ given in Eqs. 3.1, the stationary values of the tyre compression (h_0), fork compression (z_0) and caster angle variation (γ_0) due to $M_{\gamma 0}$ and $M_{\vartheta 0}$ are immediately found by:

$$\begin{cases} h_0 & = k_r^{-1} F_{\eta 0} \\ z_0 & = k_z^{-1}\left[\left(F_{\eta 0} - mg\right)\hat{c}_0 - F_{\xi 0}\hat{s}_0\right] \\ \gamma_0 & = k_\gamma^{-1}\left\{\left(F_{\eta 0} - mg\right)\left[x_f \hat{c}_0 + \left(l - z_0\right)\hat{s}_0\right] + \right. \\ & \quad \left. + F_{\xi 0}\left[R - h_0 - x_f \hat{s}_0 + \left(l - z_0\right)\hat{c}_0\right]\right\} \end{cases} \tag{3.17}$$

Consequently, the values of the braking and pitching moments ($M_{\vartheta 0} > 0$, $M_{\gamma 0} < 0$) are obtained by:

$$M_{\vartheta 0} = -r_0 F_{\xi 0}, \quad M_{\gamma 0} = k_\gamma \gamma_0 \tag{3.18}$$

The model is then linearized by Taylor expansion of Eqs. 3.7–3.8, including the simplifications due to the static equilibrium (Eqs. 3.17), yielding the equations of motion in the form:

$$\mathbf{M}\ddot{\mathbf{q}} + \mathbf{C}\dot{\mathbf{q}} + \mathbf{K}\mathbf{q} = \mathbf{0} \quad \text{with} \quad \mathbf{q} = \left\{\begin{array}{ccc} \gamma & z & \vartheta \end{array}\right\}^{\mathbf{T}} \tag{3.19}$$

where the $\mathbf{M}$, $\mathbf{C}$ and $\mathbf{K}$ matrices have the following expressions:

$$\begin{aligned} \mathbf{M} &= \begin{bmatrix} m(x_f^2 + z_{f0}^2) + J_{12} & m x_f & 0 \\ m x_f & m & 0 \\ 0 & 0 & J_3 \end{bmatrix} \\ \mathbf{C} &= \begin{bmatrix} c_\gamma & 0 & 0 \\ 0 & c_z & 0 \\ 0 & 0 & 0 \end{bmatrix} + A \begin{bmatrix} \eta_0^2\left(1 + \kappa_0\right) & -\eta_0 \hat{s}_0\left(1 + \kappa_0\right) & \eta_0 R \\ -\eta_0 \hat{s}_0\left(1 + \kappa_0\right) & \hat{s}_0^2\left(1 + \kappa_0\right) & -\hat{s}_0 R \\ \eta_0 r_0\left(1 + \kappa_0\right) & -\hat{s}_0 r_0\left(1 + \kappa_0\right) & r_0 R \end{bmatrix} \\ \mathbf{K} &= \begin{bmatrix} k_\gamma - (k_r h_0 - mg)\eta_0 + \left(F_{\xi 0} + k_r \xi_0\right)\xi_0 & (k_r h_0 - mg)\hat{s}_0 + \left(F_{\xi 0} + k_r \xi_0\right)\hat{c}_0 & 0 \\ (k_r h_0 - mg)\hat{s}_0 + \left(F_{\xi 0} + k_r \xi_0\right)\hat{c}_0 & k_z + k_r \hat{c}_0^2 & 0 \\ -F_{\xi 0}\xi_0 & -F_{\xi 0}\hat{c}_0 & 0 \end{bmatrix} \\ & \quad - B \begin{bmatrix} \xi_0 \eta_0 & \eta_0 \hat{c}_0 & 0 \\ -\xi_0 \hat{s}_0 & -\hat{s}_0 \hat{c}_0 & 0 \\ \xi_0 r_0 & \hat{c}_0 r_0 & 0 \end{bmatrix} \end{aligned} \tag{3.20}$$

The equilibrium–state speed V_0 explicitly affects only coefficient A. Matrix $\mathbf{K}$ is highly non–symmetric, which can bring the system to instability.

3.2 Stability analysis

Stability of the linearized minimal model is studied in equilibrium configurations by means of sensitivity analysis with respect to the model's governing parameters. Stability maps are drawn on the basis of sets of parameter values related to a straight running braking manoeuvre performed by a road racing motorcycle. Results are compared with those found in the literature [1,3,5] and with those obtained by a multibody planar motorcycle model, in this case also considering transient braking manoeuvres. The source of the self–excited vibration is investigated by means of phase–diagrams of the unstable mode at the stability threshold, aimed at explaining its driving mechanism and at identifying which parameters play a major role in the actual vibration onset.

3.2.1 Stability maps

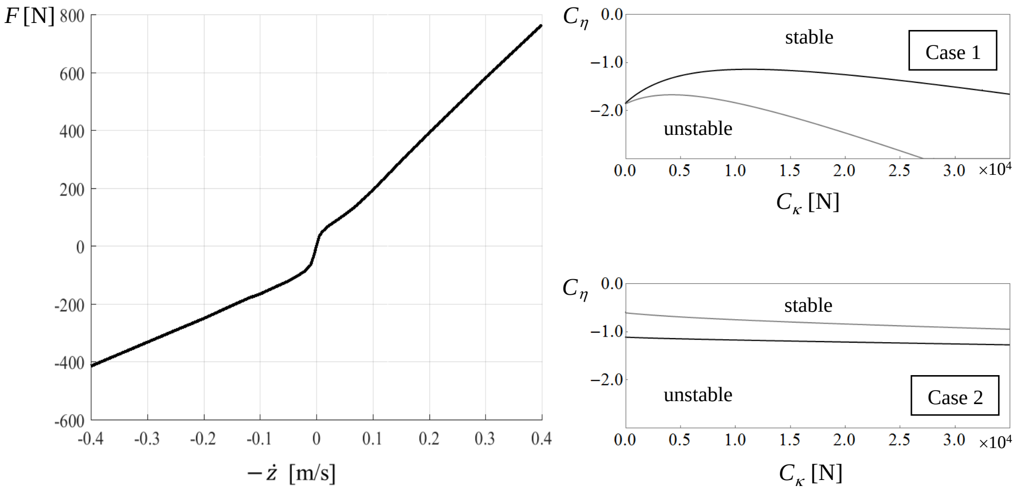

Figure 3.2: Characteristic function of the front suspension viscous damper (left) and stability maps in the plane (C_κ, C_η), with parameters as in Table A2 (right); black thresholds computed with linearized c_z, gray thresholds computed with averaged c_z.

Stability maps are obtained by applying the Routh–Hurwitz criterion to the characterisitc equation descending from Eqs. 3.19, using the symbolic algebra software. A set of values is adopted for the model parameters, related to a straight running, steady–state, braking manoeuvre performed by a road racing motorcycle, considering two very different positions of the fictitious center of rotation P: in the first case (in the following referred to as "case 1") point P is positioned such as the angular displacement γ were totally due to pitch rotation of the motorcycle's main frame (parameters reported in Table A2); in the second case (in the following referred to as "case 2") point P is positioned close to the steering axis such as γ were only due to angular compliance of the upper front assembly with respect to the main frame, as assumed in [3] (modified parameters with respect to case 1 are reported in the Appendix, at Table A2). In particular, in both cases the position of P and the values of J_{12} and k_γ are inferred from multibody analysis of the planar motorcycle model adopted in Section 3.2.2, in order to make the minimal model as consistent as possible with the full motorcycle one. Clearly, in real motorcycles the actual, non–stationary value of caster angle would result from a combination of the two opposite idealizations represented by cases 1 and 2, their relative importance depending on the stiffness of the frame assembly.

The non–linear damping characteristic function of the front suspension, adopted in both the minimal and multibody models, is displayed in Figure 3.2 (left): it is an almost piecewise linear function, consisting of a typical bi–linear characteristic function modified by a very steep intermediate gap (due to Coulomb friction effects). If linearized in the origin, it yields an extremely high value ($c_z = 7000$ Ns/m, in the following referred to as "linearized c_z"), much more than its average value computed without considering the intermediate step ($c_z = 1470$ Ns/m, in the following referred to as "averaged c_z"). Coulomb friction in the forks may be included in the model by modifying the characteristic function of the front suspension, with the effect of increasing further the slope of the intermediate step.

As it will be clarified, a convenient representation for the stability maps is the (C_κ, C_η) plane, as shown in Figure 3.2 (right), drawn for case 1 (top) and case 2 (bottom) adopting the values reported in Table A2 (with both linearized and averaged c_z). Since the stability thresholds in the $C_\eta > 0$ region are not of practical interest for this study, they will not be considered.

For small absolute values of C_η the system is always stable, while the stability region (smaller in case 2), at least for medium–high values of C_κ, in

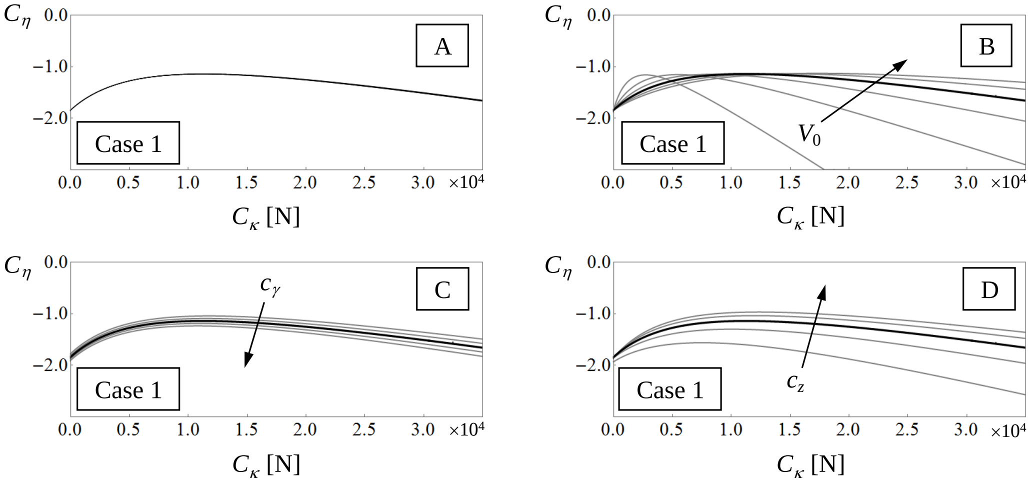

Figure 3.3: Stability maps, parameters as in Table A2 (case 1, with linearized c_z); effects of: braking manoeuvre (A); travelling speed V_0 (B); damping coefficients c_γ (C) and c_z (D).

both maps widens with increasing C_κ. In fact, for every fixed value of travelling speed V_0, increasing C_κ means increasing the damping matrix coefficient A in Eqs. 3.19. On the other hand, since $(C_\eta k_r)$ represents the dominant component in the stiffness coefficient B (Eqs. 3.16), increasing the absolute value of C_η means increasing the highly non–symmetric B–component of the stiffness matrix, bringing the system towards instability [38, 5].

Case 1 is considered first. The results of a sensitivity analysis involving parameters which are dependent on specific manoeuvres are displayed in Figure 3.3 (A, B), where black curves identify the stability thresholds computed with parameters as in Table A2 (linearized c_z). A braking manoeuvre is considered, consisting of a sequence of steady–state braking equilibrium conditions, all at the same travelling speed V_0 (parameters which vary in the manoeuvre are reported in Table A2; other parameters, like κ_0, do not vary significantly). The effects on the stability threshold can be regarded as negligible (plot A), which is confirmed by an analogous analysis performed considering separately all the involved parameters (including the longitudinal slip κ_0, whose direct effect in Eqs. 3.19 is negligible in any case). On the contrary, the travelling speed V_0 is highly influential, with a destabilizing effect at medium–high values of C_κ which grows considerably with C_κ (plot B, computed with V_0 = 50, 100, 150, 200, 250, 300 km/h). Therefore the only really relevant manoeuvre–dependent parameters for this stability analysis are the components of the tyre characteristic gradient (C_κ, C_η) and the travelling speed V_0. This means that the manoeuvre–dependent variations of structural parameters of the motorcycle (like the one shown in Table A2 for stiffness k_z) are not really influential on stability. Hence, in this respect, (given) structural parameters can be regarded as manoeuvre–independent. Which explains the choice of representing stability maps on the (C_κ, C_η) plane, or alternatively on the ($A = C_\kappa\ /V_0$, C_η) plane, providing a complete picture of manoeuvre effects, each point related to a combination of input parameters ($M_{\vartheta 0}$, $M_{\gamma 0}$, V_0).

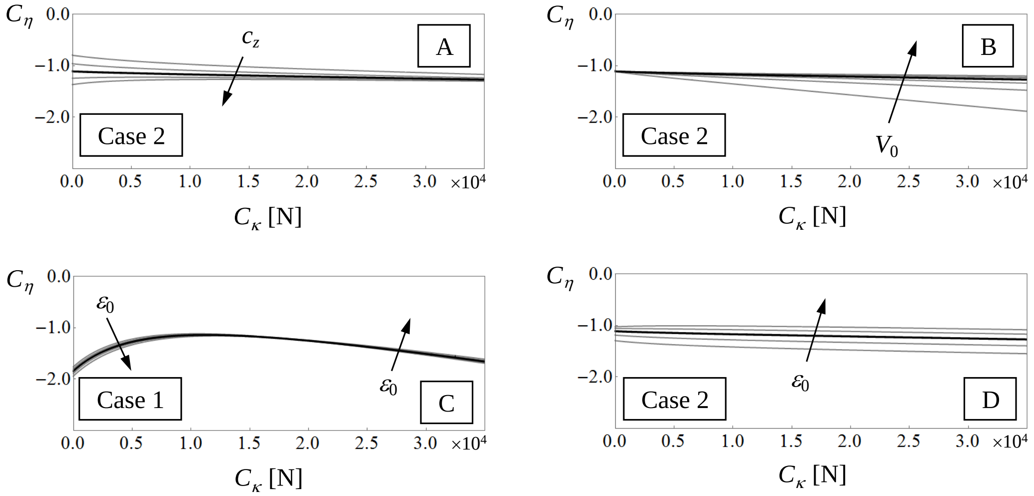

Figure 3.4: Stability maps, parameters as in Table A2 (case 2, with linearized c_z); effects of damping coefficient c_z (A) and travelling speed V_0 (B). Effects of large variations of caster angle ε_0: case 1 (C) and case 2 (D).

The results of sensitivity analysis involving parameters independent from manoeuvres, specific of the motorcycle itself, are displayed in Figure 3.3 (C, D), where black curves identify the stability thresholds computed adopting the parameter values reported in Table A2, with linearized c_z and related equivalent damping coefficient $c_\gamma = 210$ Nms/rad (inferred from the multibody model analysis, as discussed in Section 3.2.2). Increasing c_γ is always stabilizing (plot C, variation of c_γ in the range ±40%), while the opposite effect is obtained by increasing c_z (plot D, variation of c_z in the range ±50%). Hence it can be concluded that an intermediate step in the damping characteristic function, due to Coulomb friction, in case 1 encourages the onset of patter vibration, with highly destabilizing effects. The separate effects of other parameters, i.e. the unsprung mass m, the wheel moment of inertia J_3, the front suspension stiffness k_z (their reduction enhances stability), the tyre radial stiffness k_r, the free rolling radius variation factor e (their increase enhances stability) and the unloaded wheel radius R (its increase enhances stability, but only at medium–high values of C_κ), if varied in a range of ±10%, were all found to be very small.

Case 2 is now considered, i.e. the effects of moving the fictitious rotation centre P towards the steering axis, and at the same time of varying J_{12}, k_γ and c_γ accordingly. The results of sensitivity analysis are shown in Figure 3.4 (A, B), where black curves identify the stability thresholds computed adopting the parameter values reported in Table A2, with linearized c_z. Increasing the front suspension damping coefficient c_z has now a moderate stabilizing effect (left, variation of c_z in the range ±50%), while increasing the travelling speed V_0 has a destabilizing effect as in case 1, even though with smaller magnitude (right, computed with $V_0 = 50$, 100, 150, 200, 250, 300 km/h). The separate effects of other parameters, if varied in a range of ±10%, also in this case were all found to be very small.

Finally, the effects of large variations of caster angle are studied for both cases 1 and 2 with linearized c_z, as shown in Figure 3.4 (C, D) varying ε_0 in a range of ±20%. To this purpose, the caster angle in Eqs. 3.20 is modified without changing the external actions ($F_{\xi 0}$, $F_{\eta 0}$) and all the other parameters but z_{f0}, which is a function of ε_0:

$$z_{f0} = \hat{c}_0^{-1}(d_0 - r_0 + x_f \hat{s}_0) \tag{3.21}$$

Modifications of the stability threshold are larger in case 2, with stabilizing effect due to reducing ε_0. In case 1, the geometric coupling between longitudinal and normal ground force components introduced by the caster angle plays a role of minor importance.

3.2.2 Comparison with a multibody planar motorcycle model

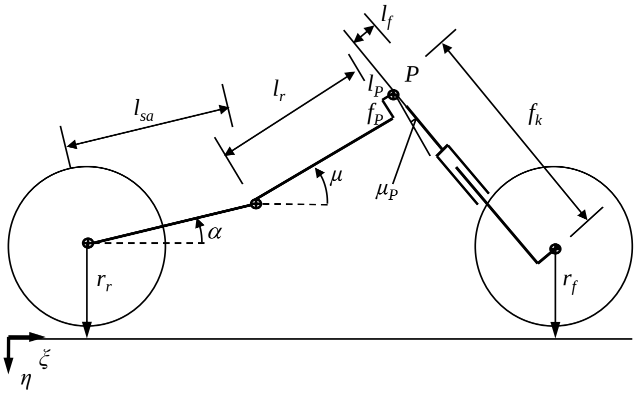

Figure 3.5: Schematic of the adopted planar multibody model.

The results of the previous analysis are compared with those obtained by a multibody planar motorcycle model. The adopted model, as sketched in Figure 3.5, is a modification of the one described in section 2.1, without considering rigid–ring tyres and introducing an additional degree of freedom for taking into account an in–plane rotation of the upper steering assembly with respect to the main frame. A deeper description of this model is given in the Appendix at A.1.12. A list of parameters, together with numerical values, is reported in Table A3 in the same Appendix; the non–linear damping characteristic function of the front suspension is the same displayed in Figure 3.2 (left), while that adopted for the rear suspension is the same as reported in Section 2.1.

A comparison between linearized models (multibody and minimal, case 1) is presented in Figure 3.6, forcing either the linearized $c_z = 7000$ Ns/m (left) or the averaged $c_z = 1470$ Ns/m (right) in both models. In the multibody model, pitching motion is damped due to additional effects other than those of the front suspension (due to rear suspension); hence an equivalent value had to be selected for c_γ in the two different cases to get the minimal model consistent as possible with the multibody one ($c_\gamma = 210$ Nms/rad, left; $c_\gamma = 95$ Nms/rad, right). In this way, the stability thresholds computed with the two models are almost superimposed.

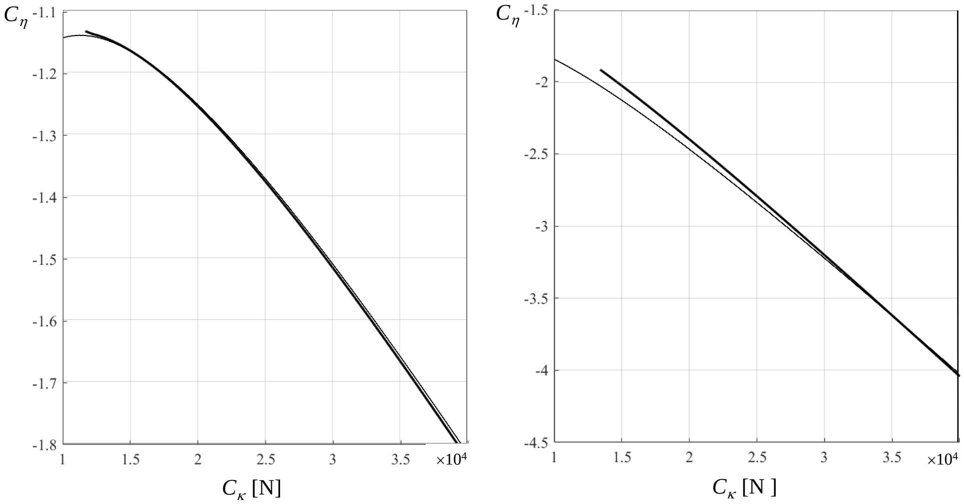

Figure 3.6: Stability maps computed with the multibody (thick lines) and minimal (case1, thin lines) models, with $c_z = 7000$ Ns/m (left; $c_\gamma = 210$ Nms/rad in the minimal model) and $c_z = 1470$ Ns/m (right; $c_\gamma = 95$ Nms/rad in the minimal model).

This suggests that all the relevant features and parameters controlling the onset and development of patter instability can be included in the minimal model, in spite of all the simplifying assumptions, as that regarding the fictitious center of rotation P.

It is also clear that in case 2 the minimal model would not be able to fit the stability thresholds computed with the multibody model, which indicates that, in case of very stiff elements and assemblies, patter vibration is mainly associated to pitch of the motorcycle's main frame, rather than to fork pivoting with respect to the frame itself.

Finally, a transient manoeuvre is simulated with the multibody model, with input data as reported in Table A3. The development of oscillations is shown in Figure 3.7 (left) in terms of wheel spindle motion with respect to stationary position. At the end of the braking manoeuvre, stability is quickly recovered due to reduction of travelling speed, and a limit cycle does not develop.

While stationary manoeuvres on (C_κ, C_η) diagrams are represented by single fixed points, transient manoeuvres are represented by time–dependent points describing trajectories. So, plotting on the same diagram a trajectory due to a transient manoeuvre, together with some selected stability thresholds computed in stationary conditions, provides some insights into the system's transient behaviour.

With the multibody model, a stationary braking manoeuvre can be generated by keeping constant both the travelling speed and the vehicle's configuration. Which can be obtained simply by imposing two independent external actions, consisting of a longitudinal acceleration and a longitudinal load transfer. A stability threshold can then be computed for the linearized model by means of the iterative procedure described at Section 2.6.

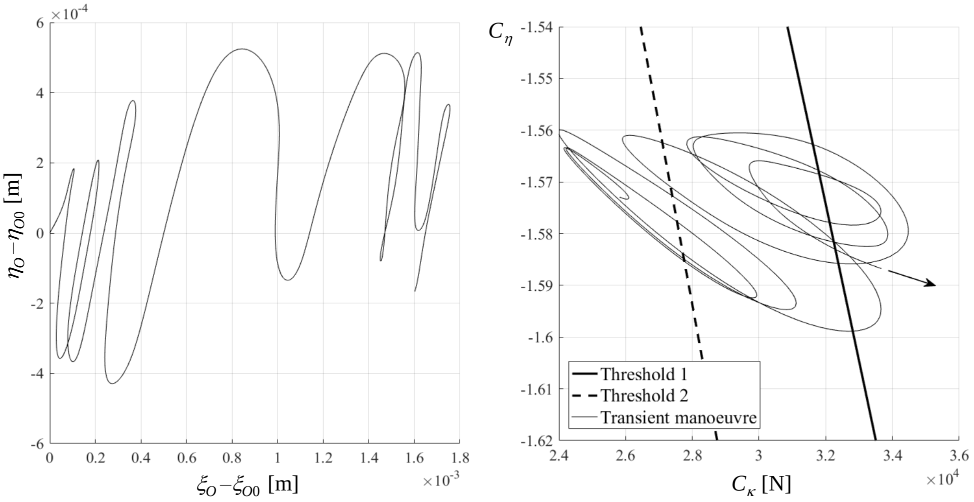

Figure 3.7: Wheel spindle motion with respect to stationary position (left) and stability map computed with the multibody model during a transient manoeuvre, showing the stationary stability thresholds at the beginning and at the end of the manoeuvre (right).

The map displayed in the right side of Figure 3.7 shows the trajectory

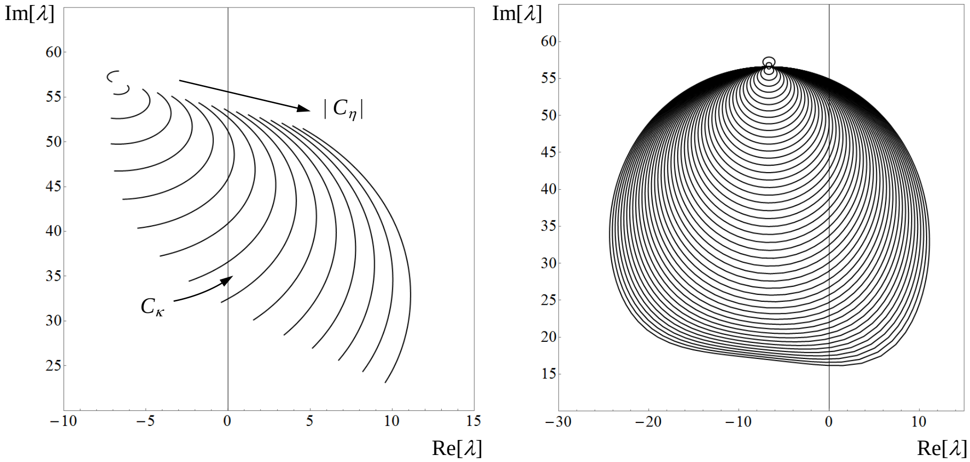

Figure 3.8: Root locus of the mode becoming unstable, varying C_κ at different fixed values of C_η (case 1). Left: $C_\kappa \in [0, 3.5 \times 10^4]$ N, $C_\eta \in [-3, 0]$. Right: $C_\kappa \in (-\infty, +\infty)$ N, $C_\eta \in [-3, 0]$.

due to the transient braking manoeuvre which originates the plot in the left side. On the same diagram, two different stability thresholds are drawn, the first one (solid line) keeping constant $V_0 = 200$ km/h (travelling speed at which, during the transient manoeuvre, patter vibration arises), the second one keeping constant $V_0 = 120$ km/h (travelling speed at which, during the transient manoeuvre, patter vibration vanishes). This suggests that during transient manoeuvres, a time–lag exists between the instant in which the trajectory crosses for the first time the stationary stability threshold on the (C_κ, C_η) diagram (at $V = V_0$), and the instant of actual vibration onset, at $V(t) = V_0$. Or, in other words, that stability margins exist beyond stationary thresholds.

3.2.3 The unstable mode

Some insights about the mode becoming unstable are reported. The minimal model herein considered (3 dofs) always yields a mode with two real eigenvalues (due to the fact that the third column of the stiffness matrix in Eqs. 3.20 has zero elements): one of them is null and the other one is negative. This mode basically corresponds to rolling of the (front) wheel, and it is always

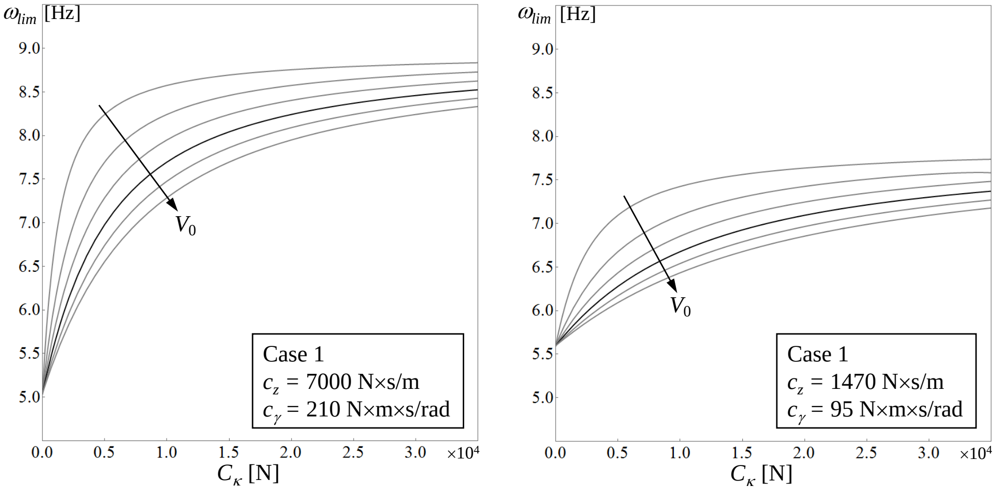

Figure 3.9: Natural frequency at different values of travelling speed ($V_0 =$ 50, 100, 150, 200, 250, 300 km/h), evaluated at the stability threshold as a function of C_κ (case 1).

stable. Among the other two modes, under the assumption of realistic finite values for damping parameters, the one which becomes unstable is always underdamped, hence the loss of stability is always oscillatory. The root locus of the model becoming unstable, drawn varying C_κ at different fixed values of C_η (covering the range of interest for the present study), is displayed in Figure 3.8 referring to the minimal model, case 1 with linearized c_z. In the left side, C_κ spans the interval $[0, 3.5 \times 10^4]$ N while C_η varies in $[-3, 0]$. In the right side, to give a more complete picture of the locus (even though exceeding realistic bounds), C_κ spans the whole interval $(-\infty, +\infty)$ N with C_η still varying in $[-3, 0]$. Clearly, instability occurs when a complex eigenvalue crosses the imaginary axis.

The natural frequency of the mode becoming unstable, evaluated with the minimal model at the stability threshold as a function of C_κ, is reported for different values of travelling speed V_0 in Figure 3.9 (case 1: left, linearized c_z; right, averaged c_z) and Figure 3.10 (case 2: left, linearized c_z; right, averaged c_z). In case 1 with linearized c_z, in the range of interest for C_κ, the natural frequency varies in an interval between 7 and 9 Hz (slightly increasing with

C_κ), consistently with data recorded on instrumented motorcycles, as shown in Figure 3.13. It can be regarded as almost independent with respect to the parameters characterizing possible braking manoeuvres, the most influential one being the travelling speed V_0, however producing variations that for medium–high values of C_κ are bounded in a range of about 1 Hz. In case 1 with averaged c_z, the natural frequency spans a different interval, between 6 and 7.5 Hz, which is too low with respect to measured data. This suggests that Coulomb friction effects in front dampers and/or forks, as that affecting the characteristic function in Figure 3.2 (left), play a relevant role in patter instability.

In case 2 (with both linearized and averaged c_z), the natural frequency varies in intervals (20–21 Hz and 12–15.5 Hz, respectively) which are neither consistent with measured data (Figs. 3.2–3.4, 3.6 and 3.7), nor with results of multibody simulations (Figure 3.14). This confirms that, in case of very stiff elements and assemblies, patter vibration is mainly associated to pitch of the motorcycle's main frame (case 1), rather than to fork pivotting with respect to the frame itself (case 2).

Histograms of the relative amplitudes of modal shape components at the stability threshold are reported in Figure 3.11 for case 1 (left) and case 2 (right), with linearized c_z. The modal shape (right eigenvector) of the mode becoming unstable, evaluated at the stability threshold, is first converted to a dimensionally homogeneous one (multiplying its γ–component by d_0 and its ϑ–component by R in both cases). Then the amplitude of each dimensionally homogeneous component is normalized with respect to the Euclidean norm of the modal shape itself, and reported in the diagram as a function of C_κ. In case 2 the mode becoming unstable is clearly dominated by the flexural compliance of frame/fork assembly (Figure 3.11 right), while in case 1 a pitch component prevails over fork travel z (Figure 3.11 left). In both cases, however, there is a strong component about rim rotation, and the relative amplitudes of the three components are almost constant with respect to C_κ (i.e. the modal shape does not vary significantly along the stability threshold).

3.2.4 Analysis of the source of instability

The switching mechanism to instability controls the energy flow in the model. If the flow from the source to the oscillator is larger than the dissipated energy during one cycle, the vibration amplitude increases. If it is smaller, the

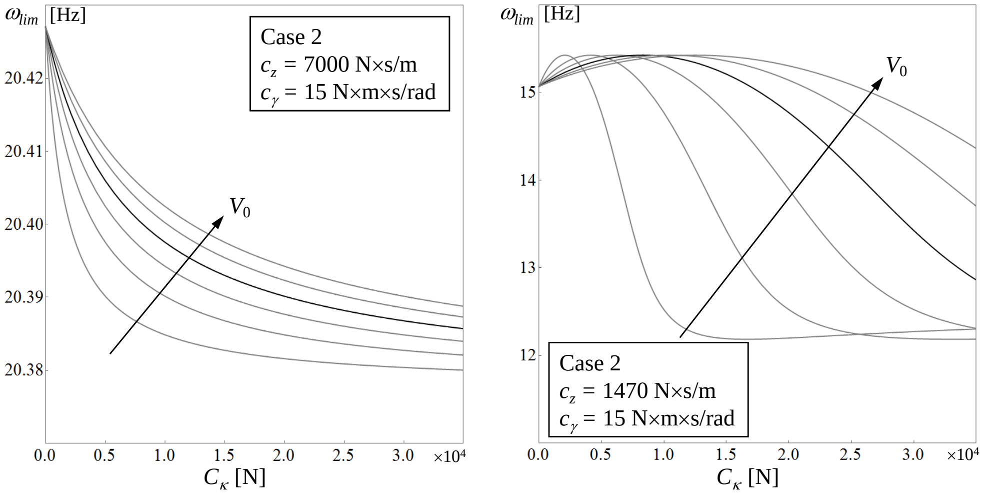

Figure 3.10: Natural frequency at different values of travelling speed ($V_0 =$ 50, 100, 150, 200, 250, 300 km/h), evaluated at the stability threshold as a function of C_κ (case 2).

amplitude decreases. At the stability threshold, the energy input balances the dissipated energy during each period [38]. In the case under study, the rate of energy supply during oscillation at any instant is given by the product of the non–stationary components of the longitudinal ground force F_ξ and slip velocity, which can also be studied by replacing the latter with the non–stationary component of the slip κ, as defined in Eqs. 3.9, 3.14 and 3.15. When this product is negative, energy is being fed to the oscillating system by the external force, and conversely. Hence the key factor for understanding the origin of the self–excited vibration under study can be recognized in the phase–lag (say ϕ) between the non–stationary components of the longitudinal ground force F_ξ and slip κ.

Recalling Eq. 3.15, it is clear that if $C_\eta = 0$, then κ and F_ξ would be in–phase ($\phi = 0$). In these conditions the model is always stable (which answers to a question left open in [3]). Increasing C_η raises ϕ, and at the stability threshold the model becomes unstable for a certain phase–lag ϕ.

If $C_\eta = 0$ and $\phi = 0$, then the phase–diagram representation in Figure 3.14 (left) would reduce to a segment centered in the origin of the axes

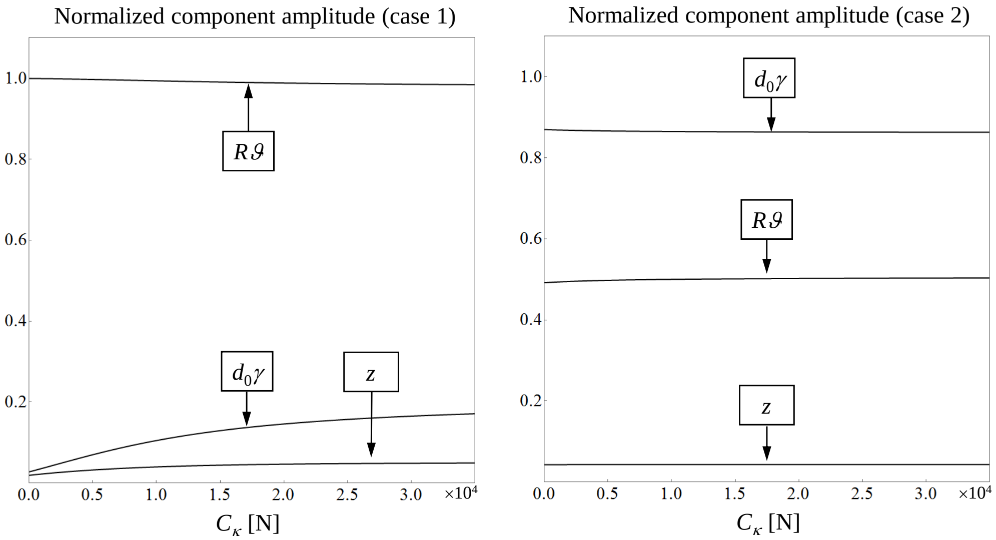

Figure 3.11: Histograms of relative amplitudes of modal shape components, evaluated at the stability threshold as functions of C_κ for both case 1 (left) and case 2 (right), with linearized c_z.

and extended in the first and third quadrants (with positive slope). In the opposite (virtual) case, κ and F_ξ would be in counter–phase ($\phi = -\pi$), hence F_ξ (κ) would be represented by a segment centered in the origin, but extended in the second and fourth quadrants (with negative slope). In the latter case the driving mechanism leading to instability would be simply given by a constitutive equation $F_\xi = c\kappa$, with $c < 0$.

The actual case is intermediate between these two extremes with constitutive equation defined by a constant coefficient, either positive or negative. In fact, the stability threshold is reached at an intermediate phase–lag ϕ, where ϕ is a function of the equilibrium point considered. The phase lag ϕ at the stability threshold is shown in Figure 3.14 (right) as a function of C_κ. It can be observed that increasing C_κ leads towards the counter–phase condition.

Then it can be stated that the key role in the switching mechanism to instability is played by C_η. It gives rise to a non–conservative restoring

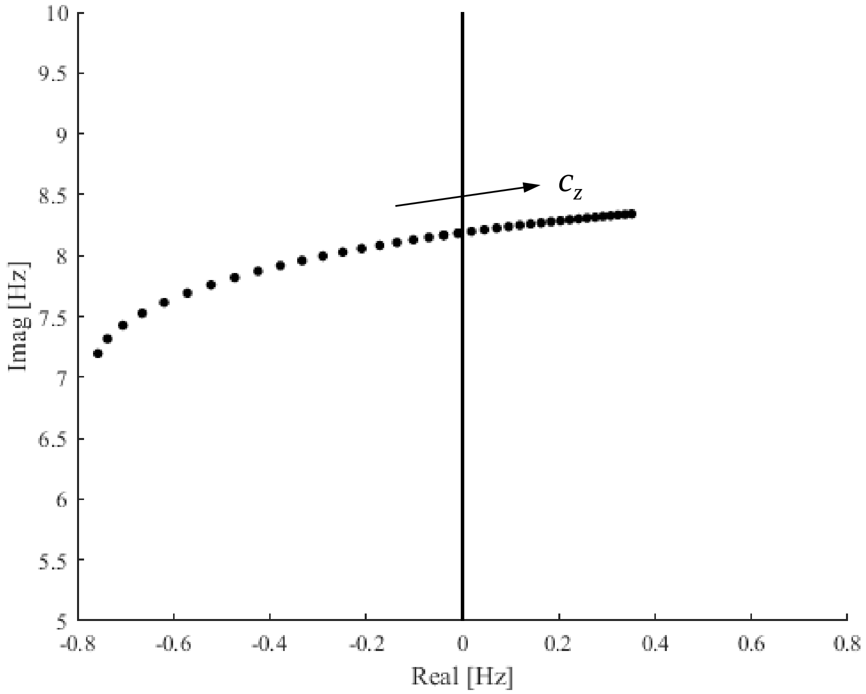

Figure 3.12: Root locus of the mode becoming unstable, as a function of linearized c_z,for the multibody full motorcycle model.

force and to an asymmetric stiffness matrix in the equations of motion 3.19, which potentially raises the phase–lag ϕ to a critical value. Basically, it is the same mechanism that generates motorcycle chatter at the rear wheel as discussed in [5, 39], differences being represented by the kind of geometrical coupling between the vertical and longitudinal oscillating forces F_ξ and F_η, and by the opposite role played by longitudinal load transfer during braking, yielding different working points on the nonlinear characteristic slip function of the tyre.

During patter vibration, the longitudinal and vertical forces F_ξ and F_η interact in two different ways: first, through the partial derivative of $F_{\xi 0}$ (κ_0,$F_{\eta 0}$) with respect to $F_{\eta 0}$ (i.e. through C_η, according to Eq. 3.15); second,

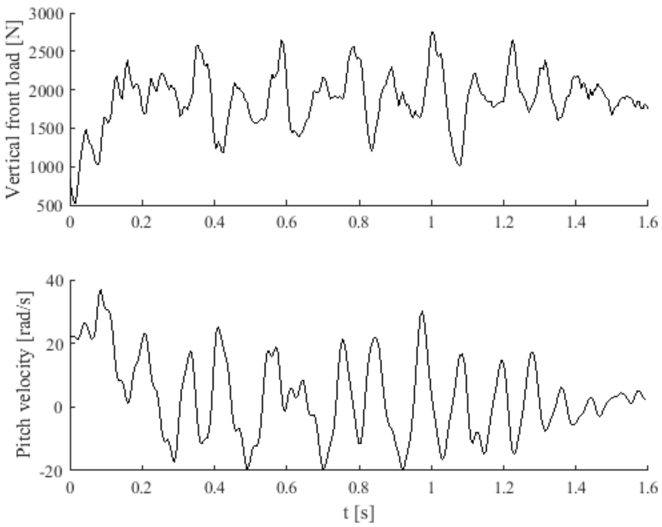

Figure 3.13: Vertical load on front wheel and main frame pitch velocity recorded as functions of time on an instrumented racing motorcycle.

as a consequence of the geometric coupling introduced by the caster angle ε_0. The former makes the occurrence of self–excited vibration possible, the latter in this case plays a secondary role.

Table 3.1: Complex eigenvalues of the full motorcycle model [Hz].

Mode	**Real Part**	**Imaginary part**
Bounce	−0.65	3.34
Pitch	−27.52	5.46
Front hop	0.00	8.18
Rear hop	−0.31	18.06
Driveline	−1.13	23.48
Flexural frame/fork assembly	−1.43	33.47

For understanding whether, in a specific case, the equilibrium points in

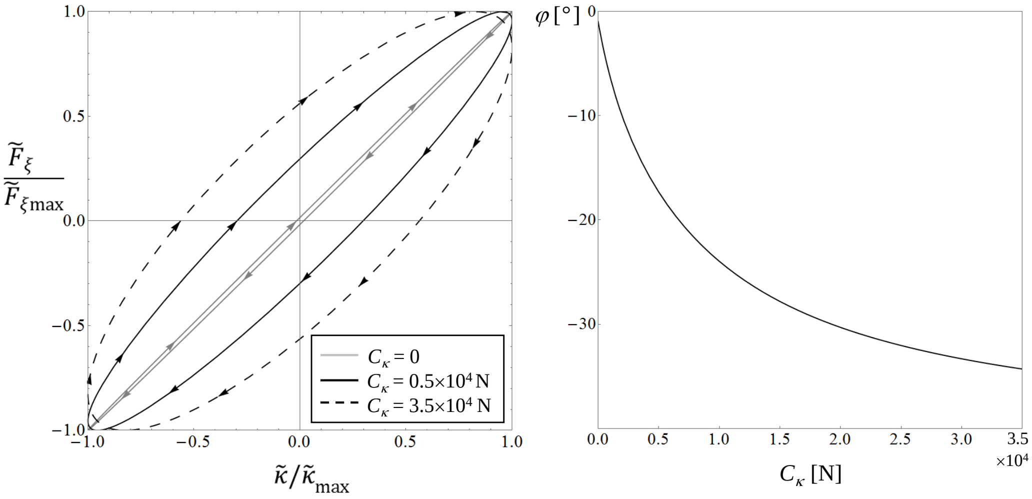

Figure 3.14: Phase–lag between longitudinal ground force and slip at the stability threshold (case 1, linearized c_z): diagram of normalized components (left) and representation as a function of C_κ (right).

the maps of Figs. 3.2–3.4, 3.6 and 3.7 are stable or not, in Figure 3.15 the gradient components C_κ and C_η as well as the braking force $F_{\xi 0}$ are represented as functions of the vertical load $F_{\eta 0}$ (with $F_{\xi 0}$ and $F_{\eta 0}$ normalized for protecting reserved data) at two different values of longitudinal slip. The only region of the diagram in which C_η gets potentially critical values takes place at high slip and high values of $F_{\xi 0}$ and $F_{\eta 0}$ (Figure 3.15, right, circled area). It can be concluded that increasing the braking torque (which means increasing both the absolute values of $F_{\xi 0}$ and $F_{\eta 0}$ leads to instability, while reducing tyre–ground friction encourages stability (since it reduces significantly C_κ, and consequently also C_η), which is a reason for racing motorcycles suffering patter vibration more than road motorcycles.

Other parameters can encourage/discourage the development of patter vibration. The travelling speed V_0 is the only other highly influential manoeuvre–dependent parameter, with strong destabilizing effects at medium–high values of C_κ. On the other hand, among manoeuvre–independent parameters, the most influential one has been recognized to be the front suspension damping. In case of very stiff elements and assemblies (patter vibration mainly associated to pitch of the motorcycle's main frame), the front suspension damping has strong destabilizing effects, enhanced primarily by the presence of Coulomb friction, and secondary by the usual asymmetry in the damping characteristic functions (the force exerted by the damper is higher in extension).

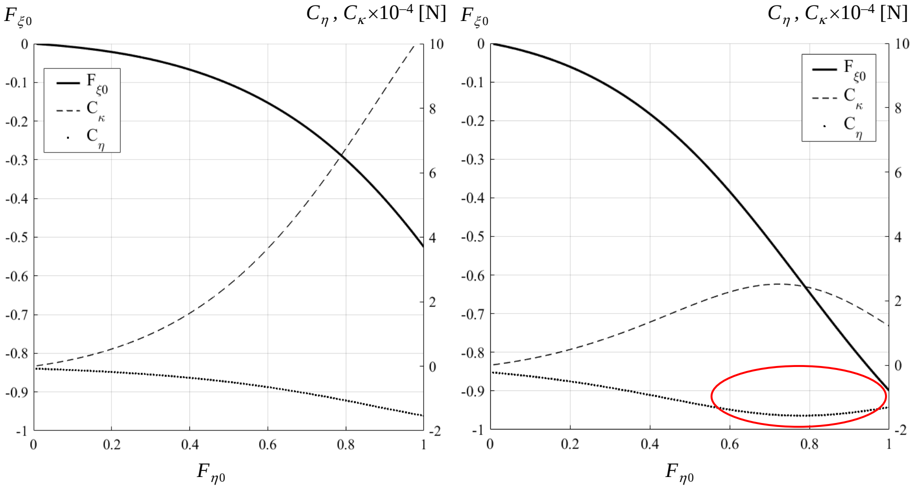

Figure 3.15: Gradient components C_κ, C_η and braking force $F_{\xi 0}$ (normalized) as functions of vertical load $F_{\eta 0}$ (normalized) at two different values (low and high) of longitudinal slip: $\kappa_0 = -1.2\%$ (left) and $\kappa_0 = -3.5\%$ (right).

Suspension damping in cases 1 and 2 has opposite effects towards stability, due to the very different position of point P. In case 2, point P is (almost) on the fork line (OS, in Figure A.1), hence oscillations in the z direction of the unsprung mass (wheel centre O) are always damped by the suspension shock absorber. This is due to the fixed constraint represented by the revolute joint in P, acting as a rigid frame to which the suspension damper is connected (exactly true if P is positioned on the fork line); therefore in this case the shock absorber acts on the mechanism basically producing an 'external damping' effect (stabilizing). In case 1, on the other hand, pitching motion would allow oscillations of the unsprung mass in z direction even in the case of locked shock absorber, which therefore acts producing an 'internal damping' effect (in some cases potentially destabilizing). As a consequence, during pitching of the frame (body 1 in Figure 3.1), suspension damping causes a periodic lifting effect on the wheel, enhancing loss of stability.

Modal analysis of the previously described multibody full motorcycle model (with parameters as in Table A3) yields results consistent with those obtained with the minimal model, case 1. Figure 3.12 displays the root locus of the mode becoming unstable, plotted varying the linearized front suspension damping (c_z) from 1470 Ns/m up to 5420 Ns/m, at a constant speed of 200 km/h. Beyond the stability threshold (reached with $c_z = 3500$ Ns/m), the unstable mode oscillates in the frequency range between 8 Hz and 8.5 Hz.

The complex eigenvalues of the multibody full motorcycle model at the stability threshold are reported in Table 3.1. It is important to notice that both the 'pitch' mode (highly damped) and the 'front hop' mode (becoming unstable) exhibit a very large component associated to front wheel rotation, together with rather large components associated to pitch of main frame as well as vertical travel of front wheel centre, consistently with the minimal model (Figure 3.11, left).

Finally, some experimental data on front wheel patter oscillation are displayed in Figure 3.13, showing vertical load on front wheel and main frame pitch velocity, recorded as functions of time on an instrumented racing motorcycle (from which the parameters reported in Table A3 and in Figure 3.2 left were taken). With a maximum braking torque of 537 N/m, a speed $V =$ 220 km/h at $t = 0$ s and a speed $V = 160$ km/h at $t = 1.6$ s, patter oscillation occurs at about 9 Hz.

Conclusions

The target of this study was to analyze the stability of the in–plane modes of a racing motorcycle, in particular referring to two of the most notorious phenomena that affect high performance vehicles, that is chatter of the rear wheel and patter of the front one. To this purpose, symbolic algebra models were developed and utilized, also with the aid of algebraic manipulating software. Stability analysis of these models was carried out using classical techniques, like time–domain simulations and eigenvalue analysis, and developing novel methods of analysis. The two unstable phenomena addressed in this work, although different from one another in terms of frequency, bodies involved and type of motion, have very significant common points. In fact, in both cases the switching mechanism of the self excitation can be identified in the reaching of a critical phase–lag between the longitudinal slip and ground force, whether relative to the front or rear tyre. As it was highlighted in the dedicated sections of this work (namely Sections 2.4 and 3.2), said phase–lag can be brought to the critical value depending on the operating point on the tyre characteristic function, in particular by the value of the partial derivatives of the longitudinal force w.r.t. the vertical force and the slip (C_η and C_κ). The nature of the switching mechanism of the self–excitation is that of a non–conservative restoring force, mathematically represented by an anti–symmetrical stiffness matrix, and practically enhanced by the inter–dependence of the longitudinal and vertical tyre–ground forces. This dependence is physically due to the tyre characteristic function, in particular parameter C_η, and by a geometric coupling represented in the chatter case by the swingarm angle, and in the patter case by the fork inclination. A more detailed description of the results obtained relatively to the two unstable phenomena is given in the following paragraphs.

Driveline instability

The unstable phenomenon known as chatter of the rear wheel, consisting in an oscillation at about 17–22 Hz of the rear motorcycle assembly, has been studied thanks to a 10–dofs full motorcycle model. The model stability has been studied first in constant velocity conditions, then during straight–line braking manoeuvre, with control input derived from data measured on an instrumented motorcycle during a real manoeuvre. The time domain integration of EoMs shows an unstable oscillatory phenomenon rising. The oscillation has the frequency of the imaginary part of the eigenvalue at the stability limit, around 22 Hz, and it consists in a counter–phase oscillation of pinion and wheel sprocket, associated to the oscillation of the rear suspension. It is noted that instability may arise even with the rear tyre keeping in contact with the ground. An interpretation of the source of instability has been given, based on the rear tyre Magic Formula parameters C_κ and C_η, representing the partial derivatives of the longitudinal force with respect to the longitudinal slip and the vertical force respectively. In the transient manoeuvre under study, it was shown how, in the first phase, the oscillation amplitude is increased by the combination of a lower and highly variable C_κ together with a high absolute value of C_η. This combination enhances instability, and is associated with a counter–phase of κ (slip) and F_ξ (longitudinal force). During the last phase of the manoeuvre, instead, an increased vertical force brings the operating point on the tyre characteristic closer to the linear portion, where C_κ varies less, while F_ξ–κ become closer to an in–phase oscillating condition, and the vibration gradually vanishes.

The differences between the system eigenvalues and eigenvectors in the conditions of constant velocity and straight–line braking have been analyzed, the most relevant being the driveline eigenvalue real part becoming positive, thus leading the system to instability. Bounds of validity of the frozen–time eigenvalues analysis have been discussed, and it was shown that in the particular application under study, the results of this technique are consistent with the self–excited vibration detected in the transient manoeuvre. However, an uncertainty appeared in regards to the central phase of the instability, when the oscillations have reached their peak amplitude and are starting to decrease. To address it, the analysis of a time–independent system has been introduced, which removes the uncertainty due to the parameters varying at a high rate.

The analysis of a time–independent system has been performed by implementing straight–line stationary braking manoeuvres; this implies applying brake torque control input while the speed of the vehicle does not change. This result has been obtained by means of fictional actions introduced in the model: a longitudinal forward acceleration that works against the braking input, and a load transfer thanks to which the typical braking configuration of the vehicle can be reproduced. The symbolic matrices of the linearized EoMs have been employed in order to study the behaviour of the system with respect to the parameters that govern the instability.

A novel technique for drawing stability margins of a linearized system has been developed. This is an iterative method based on an application of the Rayleigh quotient, to be used if the complexity of the model makes it difficult to directly apply the Routh–Hurwitz criterion. Consistency of this method with the time–domain analysis has been documented. It was also shown how the stability margin obtained with this method on the $C_\kappa - C_\eta$ plane correlates with the trajectory of the time–domain manoeuvre in the same plane: the unstable phenomenon in the time domain originates in the unstable region of the diagram identified by the iterative method.

The results of both time domain integration and modal analysis have been compared to those obtained with a simplified (3 dofs) model in [5]; consistent response of the two models was shown. Finally, the stability margin of the two models were compared, showing consistent behaviour with respect to the two key parameters C_κ, C_η, and confirming that the proposed method for stability margin agrees with the Routh–Hurwitz criterion employed in [5].

Front wheel patter instability

In order to analyze the unstable phenomenon known as front wheel patter, a minimal model has been adopted and validated using the full motorcycle planar multibody model. The simplified model, representing a motorcycle front end, i.e. front suspension and wheel, pivoted to an ideal translating frame with infinite mass and inertia, yielded patter vibration in the frequency range between 7 and 9 Hz, consistently with data analysis on instrumented motorcycles. The switching mechanism to instability of the self–excited vibration has been identified together with its governing parameters.

Analysis of this instability gave comparable results with the driveline instability analysis of the previous chapter. Even in this case, it has been found that the key role in the switching mechanism to instability is played by the local dependency of the longitudinal ground force by the downforce (partial derivative at the equilibrium point C_η), but in this case all the quantities are relative to the front wheel of the motorcycle. Parameter C_η gives rise to a non–conservative restoring force and to an asymmetric stiffness matrix in the equations of motion, which potentially raises to a critical value the phase–lag between the non–stationary components of longitudinal ground force and slip. Beyond this limit the energy flux is reversed, with the external braking force feeding the oscillating system. As a consequence, increasing the braking torque leads to instability, while reducing tyre–ground friction has stabilizing effects.

Sensitivity analysis has clarified which, among other parameters, can encourage/discourage the development of patter vibration. The only other highly influential manoeuvre–dependent parameter has been identified in the travelling speed V_0, increasing which can have strong destabilizing effects. The center of rotation of the 3 dofs model about the inertial frame was set to two different positions, to simulate in the first case a pitch–like motion ("case 1"), and in the second one a bending of the front suspension forks ("case 2"). Among manoeuvre–independent parameters, the most influential one has been recognized to be the front suspension damping, which has two opposite effects in case 1 and 2. When the vehicle has very stiff elements and assemblies, as for racing motorcycles, patter vibration has been found to be mainly associated to pitch of the main frame (as modeled case 1), rather than to fork pivoting with respect to the frame itself. In these conditions, the front suspension damping has a strong destabilizing effect, enhanced primarily by the presence of Coulomb friction in dampers and/or forks.

Appendix A

A.1 Full multibody model description

This Appendix gives a complete description of the full motorcycle multibody models employed in this work.

The models represent a standard racing motorcycle, with final chain transmission, front telescopic fork suspension and rear pivoted swingarm suspension.

The models employed in chapter 2 and 3 share most of the features. A general description of these characteristics is given in sections A.1.1 to A.1.11, while section A.1.12 gives an explanation of the differences between the models.

A.1.1 Motorcycle model geometry

A two-dimensional multibody motorcycle model is adopted, featuring planar rigid–ring tyres with Magic Formula (MF), chain transmission for both braking and traction phases, and full drivetrain inertia.

The degrees of freedom of the proposed model are described in Table A.1. The equations of motion (EoMs) are obtained symbolically, by means of an open–source multibody library developed in Maple. The kinematic description makes it possible to evaluate the Lagrangian function L and to write the EoMs as:

$$\mathbf{M}(\mathbf{q})\ddot{\mathbf{q}} = -\mathbf{f}(\mathbf{q}, \ddot{\mathbf{q}}) \tag{A.1}$$

where $\mathbf{M}(\mathbf{q})$ denotes the mass matrix of the system and $\mathbf{f}(\mathbf{q}, \dot{\mathbf{q}})$ a vector containing all the terms proportional to displacements and velocities.

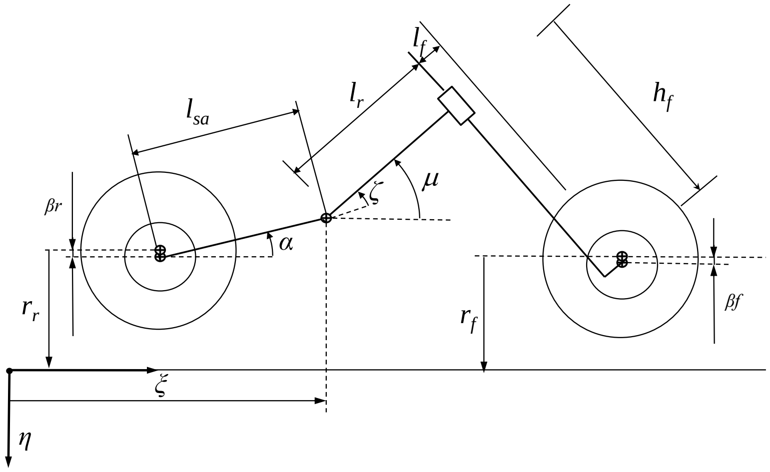

Figure A.1: Schematic of the motorcycle model.

A.1.2 Geometric parameters

The motorcycle geometry is described by means of three fixed parameters, with the dimensions of a length:

- l_{sa}, swingarm length: the distance between the rear wheel axle and the swingarm pivot
- l_r, length of the frame line: the length of a line perpendicular to the steering axis passing through the swingarm pivot
- l_f, front fork offset: the distance between the steering axis and the front wheel axle [40]

A.1.3 Independent coordinates

The motorcycle internal configuration can be defined by means of two time dependent variables: the pitch angle α of the swingarm and the pitch angle μ of the frame line, both defined with respect to the inertial reference system.

Table A.1: Degrees of freedom of the proposed motorcycle model.

	Name	DoF
1	ξ	Pivot longitudinal displacement
2	μ	Frame line pitch
3	α	Swing arm pitch
4	θ_c	Rear wheel angular displacement
5	θ_p	Pinion angular displacement
6	θ_a	Front wheel angular displacement
7	r_r	Rear wheel deformed radius
8	r_f	Front wheel deformed radius
9	β_r	Rear rim-ring displacement
10	β_f	Front rim-ring displacement

The motorcycle kinematics are derived in a planar, ξ–forward, η–down reference system, starting from the position of the swingarm pivot, which is reached with a translation of components $(\xi, 0, -r_r - l_{sa}\sin(\alpha))$, where ξ is the longitudinal position of the pivot and r_r is the rear wheel deformed radius. This definition yields the position of the rear wheel axle as: $(\xi - l_{sa}\cos(\alpha), 0, -r_r)$, and the position of the steering head as $(\xi + (l_r + l_f)\cos(\mu), 0, -r_r - l_{sa}\sin(\alpha) - (l_r + l_f)\sin(\mu))$. Note that in this planar configuration the caster angle equals the frame absolute pitch angle μ.

A.1.4 Closure equation

Defining the front wheel deformed radius as an independent variable r_f, makes it possible to obtain the closure equation in the form:

$$h_f = \frac{r_r - r_f + (l_r - l_f)\sin(\mu) + l_{sa}\sin(\alpha)}{\cos(\mu)} \tag{A.2}$$

where h_f is the front suspension extension (i.e. the distance between the steering head and the front wheel axle).

A.1.5 Rigid bodies

The model, as sketched in Figure A.1, consists of eleven rigid bodies. Each body has constant mass and moment of inertia about an axis perpendicular to the model plane. The eleven bodies are listed below, each one with a list of the real bodies it represents:

- *main body*: frame and all part that can be considered fixed with respect to it, rider, engine block, fuel tank
- *swingarm body*: swingarm, rear brake caliper, part of the lever system that acts on the rear suspension
- *steer body*: upper steering assembly, handles, fork outer tubes
- *front body*: lower front assembly comprising fork lower part, front brake calipers, fender
- *front wheel body*: front rim, brake discs, inner part of the front tyre
- *rear wheel body*: rear rim, brake discs, inner part of the rear tyre, rear wheel sprocket
- *front ring body*: front tyre excluding the inner part
- *rear ring body*: rear tyre excluding the inner part
- *crankshaft body*: crankshaft, flywheel, alternator and auxiliaries
- *main shaft body*: main gearbox shaft and clutch
- *drive sprocket body*: secondary gearbox shaft, pinion

The rider is considered fixed with respect to the mainframe, in a braking configuration: the center of gravity (CoG) of the suspended mass and the aerodynamic coefficients are set accordingly.

A.1.6 Controls

The controls applied to the model are the three torques listed below:

- M_{bf}: Front brake torque, applied to the *front wheel body* and reacting on the *front body*
- M_{br}: Rear brake torque, applied to the *rear wheel body* and reacting on the *swingarm body*
- M_e: Engine torque, applied to the *crankshaft body* and reacting on the *main body*

the front and rear brake torques (M_{bf}, M_{br}) and the engine torque (M_e).

A.1.7 Internal forces and torques

The forces and torques mutually acting among the model bodies are the following:

- F_{fk}: Fork force: acting on the *steer body* and reacting on the *front body*
- M_{sh}: Rear suspension torque: acting on the *swingarm body* and reacting on the *main body*
- F_{ch}: Chain force, acting on the *drive sprocket body* and reacting on the *rear wheel body*

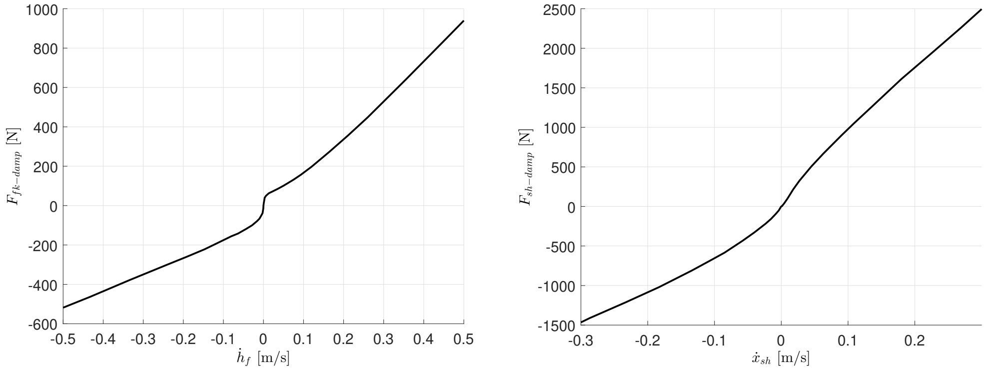

Figure A.2: Velocity-force characteristic curves for the fork (left) and shock (right) dampers.

The suspension characteristics are the sum of a displacement-dependent elastic contribution and a velocity-dependent damping contribution. The elastic component can be approximated by means of a tri–linear spring characteristic, modelling the main spring, the bottom–out bumper and the top-out spring. The damping characteristic is also non-linear, and it is modeled as a velocity-dependent force as shown in Fig. A.2. Both the elastic and damping contributions of the suspension forces are derived from experimental measurements performed by the manufacturer.

In the front suspension case, the variable controlling the suspension fork is h_f, i.e. the distance between the geometric steering head and the front rim center. Hence, the front fork force can be expressed in the form:

$$F_{fk} = f(h_f, \dot{h}_f) \tag{A.3}$$

As it pertains to the rear suspension, the independent variables in the characteristic equation are the suspension displacement (say, x_{sh}) and its first derivative w.r.t. time. A further effort is needed in order to model the rear suspension, since the actual rear suspension of the motorcycle is composed by a lever system connected to the swingarm and the main frame, which acts on the rear spring and damper. The inclusion of this system in the full multibody model would require additional closure equations and bodies with low mass, that would increase significantly the computational effort without bringing substantial improvement in the dynamics modelling. In order to keep a lower computational effort, the suspension system is modeled with a torque acting between the swingarm and the main frame. The equivalence between the rear shock force (as measured by the manufacturer) and the torque to be applied in the model are computed thanks to the principle of virtual work:

$$M_{sh}\delta\zeta = F_{sh}\delta x_{sh} \tag{A.4}$$

where F_{sh} is the rear suspension force and ζ is the angle between the frame line and the swingarm line, defined as:

$$\zeta = \mu - \alpha \tag{A.5}$$

A.1.8 External forces and torques

The external actions acting on the model bodies are of two different natures: aerodynamic and contact forces.

- F_{drag}, F_{lift}, M_{aero}: Forces of aerodynamic drag and lift, applied to the *main body* at an intermediate point at ground level, and aerodynamic torque

- $F_{\xi-f}$, $F_{\xi-r}$: front and rear longitudinal tyre-ground forces, applied to the *front rim* at the ground contact point

- $F_{\eta-f}$, $F_{\eta-r}$: front and rear vertical tyre-ground forces, applied to the *rear rim* at the ground contact point

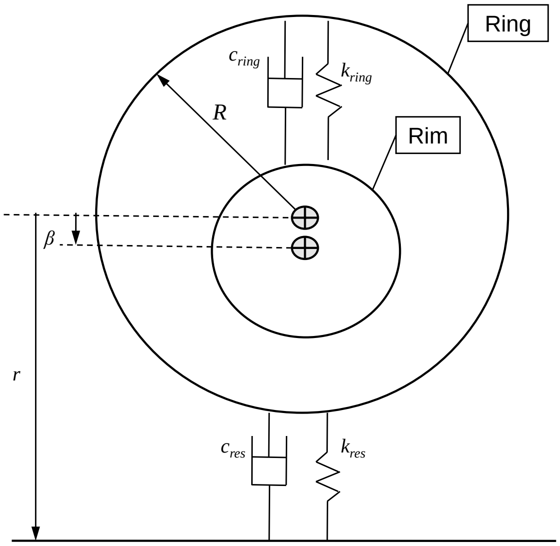

Figure A.3: Schematic of the rigid ring model.

A.1.9 Rigid ring tyre model

The tyre are modeled with two-bodies system called ”Rigid ring”, as displayed in Fig. A.3: the first body (rim) has the inertial properties of the real rim and the inner part of the tyre, supposed fixed. The second body is an outer *ring* which represents the body of the tyre.

The two bodies are connected by means of a linear sping-damper parallel system (Kelvin-Voigt type), with parameters k_{ring}, c_{ring}. Between the ring and the ground, a second Kelvin-Voigt model is present, with parameters k_{res}, c_{res}; both spring-damper systems are defined in the non-rotating reference system. The forces F_{ring} between the ring and rim are expressed in the form:

$$F_{ring} = k_{ring}\beta(t) + c_{ring}\dot{\beta}(t) \tag{A.6}$$

both for the front and rear tyres, where $\beta(t)$ is the relative displacement between the ring and rim centers.

The vertical ground forces between the ring and the inertial system are given by an expression in the form:

$$F_\eta = k_{res}(R - r(t)) + c_{res}\frac{d}{dt}(R - r(t)) \tag{A.7}$$

where R is the undeformed outer radius of the tyre and $r(t)$ (with subscript r or f according to the rear and front tyres) is the displacement from the ring center to the ground.

The value of the k_{res} parameter is descending from the assumption that the two Kelvin-Voigt models in series must have an equivalent stiffness equal to the actual radial tyre stiffness (say, k_{rad}). Hence, the value of k_{res} descends by the formula for stiffness in series, and reads:

$$k_{res} = \frac{1}{\frac{1}{k_{rad}} - \frac{1}{k_{ring}}} \tag{A.8}$$

A.1.10 Magic Formula

A motorcycle wheel is composed of two parts: a rim, which can be supposed rigid, and a deformable pneumatic tyre. Say R the external undeformed tyre radius; when the wheel moves in its middle plane with a pure rolling motion on a flat surface, its center is a at a distance a from the ground and moves forward with a velocity v_ξ. It can be identified the center of instantaneous rotation C_0 of the rim, which has a distance R_0 from the rim center, intermediate between the deformed and undeformed radius: $a < R_0 < R$. When a torque is acting on the rim, its center of instantaneous rotation C is at a distance R_c from the rim center; in case the torque is braking, then $R_c > R_0$. The velocity of point C_0 is named "longitudinal slip velocity" and it descends from the fundamental equation:

$$v_{s\xi} = \Omega R_c - \Omega R_0 \tag{A.9}$$

where Ω is the angular velocity of the rim. In this equation, the first term on the right hand side represents the velocity in the inertial system of reference of a point initially coinciding with C_0 and belonging to a non-rotating system of reference, while the second term represents the velocity of point C_0 w.r.t. the rim center in the rotating system of reference.

When an experimental evaluation of the rolling radius of the wheel is available, it can be defined the longitudinal slip factor (or simply *slip*) as:

$$\kappa = -\frac{v_{s\xi}}{v_\xi} = -1 + \frac{\Omega R_0}{v_\xi} \tag{A.10}$$

The longitudinal slip is defined as positive when the torque applied to the rim is positive, hence accelerating the vehicle. It is generally expressed as a percentage value.

The tyre longitudinal force F_ξ is derived using the well-known Magic Formula approach. According to MF 6.2, its general expression reads:

$$F_\xi = D\sin(C\arctan(B\kappa - E(B\kappa - \arctan(B\kappa)))) \tag{A.11}$$

where the slip coefficient κ is evaluated using experimentally measured values for the tyre rolling radius as a function of the forward speed of the vehicle. In particular, coefficients B, C, D take into account the dependency of the longitudinal force with the vertical load acting on the contact patch. Parameter D sets the maximum grip available, while the product BCD expresses the slope of the characteristic curve at the origin, in the form (considering unit scaling factors):

$$K_\xi = \left.\frac{\partial F_\xi}{\partial \kappa}\right|_{\kappa=0} = BCD = F_\eta(p_{Kx1} + p_{Kx2}\Delta F_\eta)e^{p_{Kx3}\Delta F_\eta} \tag{A.12}$$

where

$$\Delta F_\eta = \frac{(F_\eta - F_{\eta 0})}{F_{\eta 0}} \tag{A.13}$$

The actual tyre slip stiffness are defined for each operating point of the tyre characteristic as:

$$C_\kappa = \frac{\partial F_\xi}{\partial \kappa} \quad C_\eta = \frac{\partial F_\xi}{\partial F_\eta} \tag{A.14}$$

The order of magnitude of C_κ for low values of slip is 10^4 N; it has maximum value for when the slip is null, and decreases to zero at the peak of the MF curve. The value of C_η is close to unity for positive values of slip, and it changes sign when the slip is negative (braking conditions).

A.1.11 Transmission model

The transmission is modeled by means of three rigid bodies representing the crank shaft, the primary and secondary gearbox shafts; each of the bodies has constant moment of inertia w.r.t. its rotation axis. The rotation of these shafts are named respectively θ_{cs}, θ_{ms} and θ_{ds}; the only independent degree of freedom is θ_{cs}, while the remaining two are computed thanks to the actual primary gear ratio and the selected gear.

The multibody model receives M_e as an input, i.e. the torque acting on the crank shaft and reacting on the *frame body.* In the actual vehicle, this action is exchanged by the two bodies by means of the engine, which is a dynamic system itself and can cause an oscillatory component in the reacting torque on the frame. In order to determine such a component, a dynamic model of the engine would be needed, but this goes beyond the scope of this work. Hence M_e is treated as an input to the model.

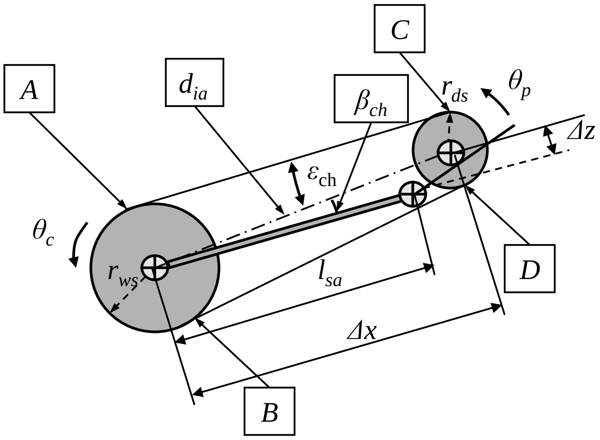

Figure A.4: Schematic of the chain transmission model.

The geometry of the final chain transmission is depicted in Fig. A.4. The pinion is fixed with the secondary gearbox shaft, and it has a radius r_{ds}. The chain is wrapped around the pinion and it transmits the motion to the rear wheel by means of the wheel sprocket, with radius r_{ws}. The final transmission ratio can be defined using these dimensions:

$$\rho_{ws-ds} = \frac{\theta_c}{\theta_p} = \frac{r_{ds}}{r_{ws}} \tag{A.15}$$

The two chain segments AC and BD, modeled as geometric linear segments, tangent to both the pinion and the wheel sprocket, have equal length that can be derived as:

$$AC = BD = \sqrt{d_{ia}^2 - (r_{ws} - r_{ds})^2} \tag{A.16}$$

where in turn the distance between the pinion and wheel sprocket centers is given by:

$$d_{ia} = \sqrt{\Delta x^2 + \Delta z^2} \tag{A.17}$$

The lengths Δx and Δz represent the coordinates of the pinion center in a system of reference with the center in the rear wheel center and the x axis parallel to the swingarm line. The direction of the two chain segments can be derived by the two angles depicted in Fig. A.4:

$$\beta_{ch} = \arctan\left(\frac{\Delta z}{\Delta x}\right) \quad \varepsilon_{ch} = \arcsin\left(\frac{r_{ws} - r_{ds}}{d_{ia}}\right) \tag{A.18}$$

The chain transmits a force parallel to the upper/lower chain segments, applied in the points A, B, C and D only when it is tight. A scheme of the chain forces and their names is depicted in Fig. A.5. Therefore, each of the chain segments is modeled as a spring that acts only in extension. To define the elastic force, the free length of the upper and lower segments are defined as given parameters l_{U0} and l_{L0}. Hence, the extensions of the two segments is calculated considering the length of AC and BD, and the wrapping of the chain around the pinion and segment, obtaining:

$$\begin{aligned} e_U &= r_{ws}\theta_c - AC - r_{ds}\theta_p + l_{U0} \\ e_L &= -r_{ws}\theta_c - BD + r_{ds}\theta_p + l_{L0} \end{aligned} \tag{A.19}$$

A viscous damper is also considered in parallel with each of the springs modeling the chain, therefore the chain force in the two segments in considered as proportional to e_U, e_L (and respective velocities):

$$\begin{aligned} F_{ch,U} &= \begin{cases} k_{ch}e_U + c_{ch}\dot{e}_U & if e_U \geq 0 \\ 0 & if e_U < 0 \end{cases} \\ F_{ch,L} &= \begin{cases} k_{ch}e_L + c_{ch}\dot{e}_L & if e_L \geq 0 \\ 0 & if e_L < 0 \end{cases} \end{aligned} \tag{A.20}$$

The total stiffness of the spring k_{ch} is evaluated taking into account the series composed by the chain (k_{l-ch}) and the sprocket torsional shock absorber

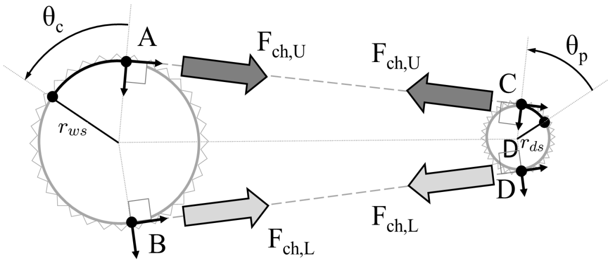

Figure A.5: Schematic of the forces acting on the chain transmission model.

(subscript ws), according to:

$$k_{ch} = \left(\frac{1}{k_{l-ch}} + \frac{r_{ws}^2}{k_{ws}} \right)^{-1} \tag{A.21}$$

The damping in the transmission may be assumed entirely due to the sprocket torsional absorber (considered linear), that is disregarding the internal damping of the chain. Hence the transmission damping c_{ch} can be expressed as:

$$c_{ch} = \frac{c_{ws}}{r_{ws}^2} \tag{A.22}$$

A.1.12 Modifications to the full multibody employed in front patter analysis

The analysis of the front patter phenomenon required an evolution of the full multibody model, which allowed to take into account the compliance of the front assembly of the vehicle. This improvement of the model would increase the overall complexity of the model to an extent that both the time-domain simulations and the model linearization would require a high computational effort. Therefore, it was decided to make a further modification to reduce the complexity of the model kinematics, with the minimum effect on the overall vehicle dynamics. It was decided to suppress the rigid ring models, since due to their high stiffness they have a dynamic effect which is more relevant at high frequencies, almost one order of magnitude higher than the phenomenon under study. The compliance on the front assembly is, in reality, due to the contribution of several flexible bodies: the main frame itself as well as

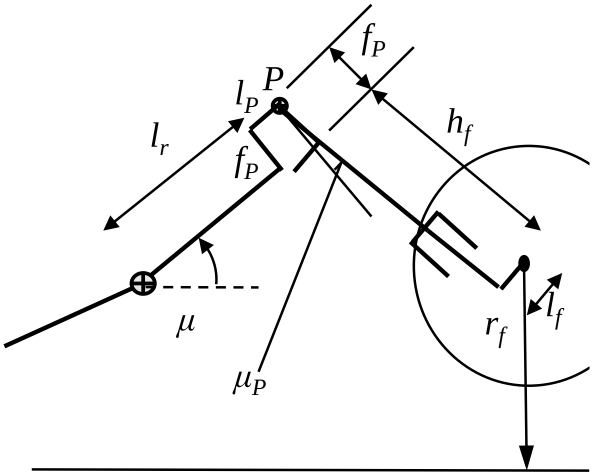

Figure A.6: Schematic of the front assembly compliance model.

the steering head and the connection elements give the major contributions. Consistently with the rest of the multibody model, a lumped-parameters approach was chosen to model the overall compliance. To define this additional model feature, the scheme of Fig. A.6 was adopted. The kinematics of the model were unvaried from the rear wheel up to the geometric steering head, which is still defined as a point with l_r distance from the pivot. Then, two additional geometric parameters are added, l_P and f_P, which represent the coordinates of the revolute joint center P, in a reference system parallel to the frame line (angle μ w.r.t. the ground line).

The additional degree of freedom μ_P represents the rotation of the fork line w.r.t. its original orientation, i.e. perpendicular to the frame line. The revolute joint in P is interposed between the *main body* and the *steer body*, therefore no additional bodies were added. The revolute joint force is defined as the sum of a linear elastic and a viscous contributions, as in a Kelvin-Voigt rotational element. Both the position of the center of compliance P and the stiffness and damping parameters resulted from static measurements of an actual motorcycle.

The fork extension h_f is now defined as the distance of the wheel center

Table A.2: Degrees of freedom of the modified full motorcycle multibody model.

	Name	DoF
1	ξ	Pivot longitudinal displacement
2	μ	Frame line pitch
3	α	Swing arm pitch
4	θ_c	Rear wheel angular displacement
5	θ_p	Pinion angular displacement
6	θ_a	Front wheel angular displacement
7	r_r	Rear wheel deformed radius
8	r_f	Front wheel deformed radius
9	μ_P	Front assembly rotation due to its compliance

from a point on the fork line at a distance f_P from point P, which allows to keep unchanged the definitions of the fork forces intensity, but it requires to substitute the closure equation A.2 with a modified version.

Due to the suppression of the rim and ring, the variable $r_f(t)$ now represents the front deformed radius, from the wheel center to the ground. Accordingly, the two former ring and rim bodies are now united in a new *wheel body*, with mass and moment of inertia equal to the the sum of the former *front wheel body* and *front ring body* parameters. It should be noted that, due to the modified model kinematics, the actual caster angle of the vehicle does not correspond to the frame line slope; in fact, the new rotation μ_P must be added to this quantity to obtain the actual caster angle.

Given the described modifications, the resulting model has the degrees of freedom expressed in table A.2, and if consists of nine rigid bodies:

- *main body*: frame and all parts that can be considered fixed with respect to it, rider, engine block, fuel tank, fuel (considered fixed with the tank)
- *swingarm body*: swingarm, rear brake caliper, part of the lever system that acts on the rear suspension
- *steer body*: upper steering assembly, handles, fork outer tubes
- *front body*: lower front assembly comprising fork lower part, front brake calipers, fender
- *front wheel body*: front wheel, brake discs

- *rear wheel body*: rear wheel, brake discs, rear wheel sprocket
- *crankshaft body*: crankshaft, flywheel, alternator and auxiliaries
- *main shaft body*: main gearbox shaft and clutch
- *drive sprocket body*: secondary gearbox shaft, pinion

Appendix B

B.1 Parameters adopted for the driveline stability analysis

A complete list of the parameters adopted for the analysis of driveline instability is provided in Table A1.

Table A1: Parameters adopted in the multibody model employed for the driveline stability analysis.

Global properties			
Motorcycle and rider mass	258.5 kg	Wheelbase	1.47 m
Center of gravity height	0.648 m	Longitudinal position of center of gravity (w.r.t. the rear axle)	0.655 m
Caster angle	0.427 rad	Trail	0.1 m
Inertial properties			
Rear rim mass	8.5 kg	Rear rim axial inertia	0.17 kgm^2
Rear ring mass	8.5 kg	Rear ring axial inertia	0.68 kgm^2
Swingarm mass	10.2 kg	Swingarm moment of inertia	0.59 kgm^2
Suspended mass including fuel and rider	205 kg	Suspended mass moment of inertia	20.5 kgm^2

Upper steering assembly mass	8.5 kg	Upper steering moment of inertia	0.23 kgm^2
Lower steering assembly mass	6.8 kg	Lower steering moment of inertia	0.2 kgm^2
Front rim mass	5.5 kg	Front rim axial inertias	0.092 kgm^2
Front rigid-ring mass	5.5 kg	Front ring axial inertias	0.35 kgm^2
Crankshaft axial inertias	0.01 kgm^2	Gearbox primary shaft axial inertias	0.15 kgm^2
Gearbox output shaft axial inertias	0.007 kgm^2		
Geometric properties			
Swingarm length	0.55 m	Frame line length	0.78 m
Steering offset	0.03 m	Rear wheel unloaded radius	0.335 m
Rear wheel torus radius	0.1 m	Front wheel unloaded radius	0.3 m
Drive sprocket radius	0.0429 m	Wheel sprocket radius	0.0934 m
Rear suspension lever ratio (static trim)	2.2		
Structural properties			
Rear suspension spring stiffness	4.2×10^4 N/m	Front suspension spring stiffness	3.2×10^4 N/m
Overall rear tyre radial stiffness (static trim)	1.78×10^5 N/m	Overall front tyre radial stiffness (static trim)	1.56×10^5 N/m

B.2 Parameters adopted for the patter stability analysis

A complete list of parameters of both the minimal model and the multibody model is provided, along with their respective values adopted for computations.

Table A2: List of parameters of the minimal model.

<table>
<tr><th colspan="4">Parameters with same value in case 1 and case 2</th></tr>
<tr><td colspan="2">Unloaded front wheel radius</td><td colspan="2">$R = 0.300$ m</td></tr>
<tr><td colspan="2">Caster angle</td><td colspan="2">$\varepsilon_0 = 0.370$ rad</td></tr>
<tr><td colspan="2">Free rolling radius variation factor</td><td colspan="2">$e = 0.9$</td></tr>
<tr><td colspan="2">Front unsprung mass</td><td colspan="2">$m = 17.6$ kg</td></tr>
<tr><td colspan="2">Front wheel moment of inertia</td><td colspan="2">$J_3 = 0.427$ kg $\times$ m^2</td></tr>
<tr><td colspan="2">Front suspension damping coefficient (linearized)</td><td colspan="2">$c_z = 7000$ Ns/m</td></tr>
<tr><td colspan="2">Front suspension damping coefficient (averaged)</td><td colspan="2">$c_z = 1470$ Ns/m</td></tr>
<tr><td colspan="2">Front suspension stiffness</td><td colspan="2">$k_z = 23516$ N/m</td></tr>
<tr><td colspan="2">Tyre radial stiffness</td><td colspan="2">$k_r = 1.5 \times 10^5$ N/m</td></tr>
<tr><td colspan="2">Frame travelling speed</td><td colspan="2">$V_0 = 55$ m/s</td></tr>
<tr><td colspan="2">Longitudinal slip</td><td colspan="2">$\kappa_0 = -0.035$</td></tr>
<tr><td colspan="2">Longitudinal ground force</td><td colspan="2">$F_{\xi 0} = -1857.3$ N</td></tr>
<tr><td colspan="2">Normal ground force</td><td colspan="2">$F_{\eta 0} = 2006.1$ N</td></tr>
<tr><th colspan="4">Parameters with different values in case 1 and case 2</th></tr>
<tr><td colspan="2"></td><th>Case 1</th><th>Case 2</th></tr>
<tr><td>Distance between fork axis and center of rotation P</td><td>$x_f =$</td><td>0.484 m</td><td>0.028 m</td></tr>
<tr><td>Distance between points O and S in the unloaded case</td><td>$l =$</td><td>0.727 m</td><td>0.615 m</td></tr>
</table>

<table>
<tr><td colspan="3">Height of center of rotation P</td><td>$d_0 =$</td><td>0.695 m</td><td>0.755 m</td></tr>
<tr><td colspan="3">Equivalent moment of inertia with respect to center of rotation P</td><td>$J_{12} =$</td><td>18.89 kg × m^2</td><td>2.26 kg × m^2</td></tr>
<tr><td colspan="3">Equivalent pitch damping coefficient (linearized c_z)</td><td>$c_\gamma =$</td><td>210 Nms/rad</td><td>15 Nms/rad</td></tr>
<tr><td colspan="3">Equivalent pitch damping coefficient (averaged c_z)</td><td>$c_\gamma =$</td><td>95 Nms/rad</td><td>15 Nms/rad</td></tr>
<tr><td colspan="3">Equivalent pitch stiffness</td><td>$k_\gamma =$</td><td>3.26 × 10^4 Nm/rad</td><td>1.25 × 10^5 Nm/rad</td></tr>
<tr><td colspan="6">Braking manoeuvre, case 1: sequence of steady-state braking conditions</td></tr>
<tr><td>Sequence</td><td>1</td><td>2</td><td>3</td><td>4</td><td>5</td></tr>
<tr><td>$M_{\theta 0}$[N × m]</td><td>483.62</td><td>510.49</td><td>537.36</td><td>564.22</td><td>591.09</td></tr>
<tr><td>$F_{\xi 0}$[N]</td><td>–1667.0</td><td>–1762.1</td><td>–1857.3</td><td>–1953.0</td><td>–2048.9</td></tr>
<tr><td>$F_{\eta 0}$[N]</td><td>1888.3</td><td>1948.9</td><td>2006.1</td><td>2069.9</td><td>2130.3</td></tr>
<tr><td>ε_0[rad]</td><td>0.377</td><td>0.374</td><td>0.370</td><td>0.367</td><td>0.363</td></tr>
<tr><td>k_z[N/m]</td><td>23373</td><td>23449</td><td>23516</td><td>23611</td><td>23696</td></tr>
</table>

Table A3: Parameters adopted in the multibody model employed for the patter stability analysis.

<table>
<tr><td colspan="4">Global properties</td></tr>
<tr><td>Motorcycle and rider mass</td><td>253.0 kg</td><td>Wheelbase</td><td>1.47 m</td></tr>
<tr><td>Center of gravity height</td><td>0.648 m</td><td>Longitudinal position of center of gravity (w.r.t. the rear axle)</td><td>0.655 m</td></tr>
<tr><td>Caster angle (static trim)</td><td>0.427 rad</td><td>Trail (static trim)</td><td>0.1 m</td></tr>
<tr><td colspan="4">Inertial properties</td></tr>
</table>

Rear wheel mass	14.7 kg	Rear wheel axial inertia	0.83 kgm^2
Swingarm mass	10.2 kg	Swingarm moment of inertia (about pivot)	1.46 kgm^2
Suspended mass including fuel and rider	205 kg	Suspended mass moment of inertia	20.5 kgm^2
Upper steering assembly mass	7.9 kg	Upper steering moment of inertia	0.23 kgm^2
Lower steering assembly mass	6.8 kg	Lower steering moment of inertia	0.1 kgm^2
Front wheel mass	9.7 kg	Front wheel axial inertias	0.427 kgm^2
Crankshaft axial inertias	0.01 kgm^2	Gearbox primary shaft axial inertias	0.15 kgm^2
Gearbox output shaft axial inertias	0.007 kgm^2		
Geometric properties			
Swingarm length	0.59 m	Frame line length	0.78 m
Steering offset	0.03 m	Rear suspension lever ratio (static trim)	2.2
Rear wheel unloaded radius	0.32 m	Front wheel unloaded radius	0.3 m
Distance between fork axis and center of rotation P (l_P)	0.028 m	Distance between frame line and center of rotation P (f_P)	0.112 m
Drive sprocket radius	0.0429 m	Wheel sprocket radius	0.0934 m
Stiffness and damping properties			
Rear suspension main spring stiffness (static trim)	4.2×10^4 N/m	Front suspension main spring stiffness (static trim)	2.3×10^4 N/m

Rear sprocket torsional stiffness	2.8×10^4 Nm/rad	Rear sprocket torsional damping	260 Nms/rad
Front assembly equivalent flexural stiffness	1.25×10^5 Nm/rad		
Tyre properties			
Overall rear tyre radial stiffness (static trim)	1.7×10^5 N/m	Overall front tyre radial stiffness (static trim)	1.5×10^5 N/m
Input parameters for the multibody transient braking manoeuvre			
Starting speed	230 km/h	Final speed	120 km/h
Maximum brake torque	590 Nm	Maximum engine brake torque	8.5 Nm

Bibliography

[1] V. Cossalter, R. Lot, and M. Massaro. "The chatter of racing motorcycles". In: *Vehicle System Dynamics* 46(4) (2008), pp. 339–353.

[2] R. S. Sharp. "The Influence of the Suspension System on Motorcycle Weave-mode Oscillations". In: *Vehicle System Dynamics* 5:3 (1976), pp. 147–154.

[3] R. S. Sharp and C. G. Giles. "Motorcycle front wheel patter in heavy braking". In: *Proceedings, 8th International Symposium of Dynamics of Vehicles on Roads and Tracks (IAVSD); Cambridge MA, USA* (1983).

[4] V. Cossalter, R. Lot, and R. Di Maggio. "The Modal Analysis of a Motorcycle in Straight Running and on a Curve". In: *Meccanica* 39 (2004), pp. 1–16.

[5] S. Sorrentino and L. Leonelli. "A study on the stability of a motorcycle wheel–swingarm suspension with chain transmission". In: *Vehicle System Dynamics* 5(11) (2017), pp. 1707–1730.

[6] L. Leonelli, N. Mancinelli, and S. Sorrentino. "A study of motorcycle chatter vibration with multibody models of increasing complexity." In: *IAVSD 2015, Graz, Austria, 17–21 August.* CRC Press. 2015.

[7] G. T. McGaw. "On the Steering of the Bicycle". In: *The Engineer* (1898), p. 557.

[8] F. J. W. Whipple. "The Stability of the Motion of a Bicycle". In: *Quart. Journ. Pure and Applied Mathematics* (1899), pp. 312–348.

[9] E. Döehring. "Steering wobble in single-track vehicles". In: *ATZ* 58(10) (1956), pp. 282–286.

[10] R. S. Sharp. "The stability and control of motorcycles". In: *Proc. Inst. Mech. Engrs. Part C* 13 (1971), pp. 316–329.

[11] R. S. Sharp. “Design for Good Motorcycle Handling Qualities”. In: *SAE Paper 972124* (1977).

[12] Y. Watanabe and K Yoshida. “Motorcycle Handling Performance for Obstacle Avoidance”. In: *SAE Paper 73033* (1973).

[13] A. Aoki. “Experimental Study on Motorcycle Steering Performance”. In: *SAE Paper 790265* (1979).

[14] D. J. Eaton. “Lateral Dynamics of the Uncontrolled Motorcycle”. In: *Proceedings of the 2nd International Congress on Automotive Safety, San Francisco.* (1973).

[15] G. E. Roe and T. E. Thorpe. “A solution of the low speed wheel flutter instability in motorcycles”. In: *Journal of Mechanical Engineering Science* 18(2) (1976), pp. 57–65.

[16] R. S. Sharp and C. J. Alstead. “The influence of structural flexibilities on the straight running stability of motorcycles”. In: *Vehicle System Dynamics* 9(6) (1980), pp. 327–357.

[17] M. K. Verma, R. A. Scott, and L. Segel. “Effect of Frame Compliance on the Lateral Dynamics of Motorcycles”. In: *Vehicle System Dynamics* 9:4 (1980), pp. 181–206.

[18] P .T. J. Spierings. “The effects of lateral front fork flexibility on the vibrational modes of straight–running single–track vehicles”. In: *Vehicle System Dynamics* 10(1) (1981), pp. 21–35.

[19] R. S. Sharp and D. J. N. Limebeer. “A motorcycle model for stability and control analysis”. In: *Multibody Syst. Dyn.* 6(2) (2001), pp. 123–142.

[20] R. S. Sharp, S. Evangelou, and D. J. N. Limebeer. “Advances in the Modelling of Motorcycle Dynamics”. In: *Multibody Syst. Dyn.* 12(3) (2004), pp. 251–281.

[21] R. S. Sharp. “Stability, Control and Steering Responses of Motorcycles”. In: *Vehicle System Dynamics* 35(4-5) (2001), pp. 291–318.

[22] R. S. Sharp and D. J. N. Limebeer. “Motorcycle steering oscillations due to road profiling”. In: *Transactions of the ASME, Journal of Applied Mechanics* 69(6) (2002), pp. 724–739.

[23] Y. Tezuka et al. "Vibration Characteristics Analysis in Vehicle Body Vertical Plane of Motorcycle during Turning". In: *Honda R&D Technical Review* 16(1) (2004), pp. 219–224.

[24] V. Cossalter, R. Lot, and M. Massaro. "The Significance of Powertrain Characteristics on the Chatter of Racing Motorcycles". In: *ASME 2012, Houston, Texas, 9–15 November*. 2012, pp. 607–613.

[25] L. Leonelli and N. Mancinelli. "A multibody motorcycle model with rigid–ring tyres: formulation and validation". In: *Vehicle System Dynamics* 53(6) (2015), pp. 775–797.

[26] G. Catania and N. Mancinelli. "Modeling nonlinear motorcycle dynamical behavior during severe acceleration and braking". In: *Proc. of the ASME International Mechanical Engineering Congress and Exposition* (2008), pp. 315–319.

[27] R. S. Sharp and Y. Watanabe. "Chatter vibrations of high–performance motorcycles". In: *Vehicle System Dynamics* 51.3 (2013), pp. 393–404.

[28] G. Catania, N. Mancinelli, and L. Leonelli. "A multibody motorcycle model for the analysis and prediction of chatter vibrations". In: *Proceedings of IMECE 2013 (IMECE paper 62903), San Diego, USA* (2013).

[29] R. S. Sharp. "The nature and prevention of axle tramp". In: *Proc. Inst. Mech. Engrs.* 184 (2A/3) (1969), pp. 41–54.

[30] C. Koenen. "The dynamic behaviour of a motorcycle when running straight ahead and when cornering". PhD thesis. TU, Delft, 1983.

[31] M. Massaro et al. "The Motorcycle Chatter". In: *BMD 2013, Tokyo, Japan 11–13 November* (2013).

[32] H. B. Pacejka. *Tyre and Vehicle Dynamics*. Butterworth–Heinemann, 2006.

[33] H. Rosenbrock. "The Stability of Linear Time–dependent Control Systems". In: *International Journal of Electronics* 15(1) (1963), pp. 73–80.

[34] I. G. Salisbury et al. "The Unification of Acceleration Envelope and Driveability Concepts". In: *IAVSD 2015, Graz, Austria, 17–21 August*. CRC Press. 2015.

[35] A. Hurwitz. “Über die Bedingungen, unter welchen eine Gleichung nur Wurzeln mit negativen reellen Theilen besitzt”. In: *Mathematische Annalen* 46(2) (1895), pp. 273–284.

[36] L. Meirovitch. *Principles and techniques of vibrations*. Vol. 1. Prentice Hall New Jersey, 1997.

[37] H. B. Pacejka. “The physics of tyre traction. Theory and experiment”. In: ed. by H. F. Hays and A. L. Browne. Springer–Verlag, 1974. Chap. Some recent investigations into dynamics and frictional behavior of pneumatic tyres, pp. 257–279.

[38] M. Kroger, M. Neubauer, and K. Popp. “Experimental investigation on the avoidance of self–excited vibrations”. In: *Philosophical Transactions of the Royal Society A* 366 (2008), pp. 785–810.

[39] L. Leonelli, S. Cattabriga, and S. Sorrentino. “Driveline instability of racing motorcycles in straight braking manoeuvre”. In: *Proc. Inst. Mech. Eng. C* (2017).

[40] A. Saccon and J. Hauser. “An efficient Newton method for general motorcycle kinematics”. In: *Vehicle System Dynamics* 47(2) (2009), pp. 221–241.

Acknowledgements

This work would not be possible without the aid and the instruments provided by the Ducati Corse DIV (Vehicle Dynamics) department, whose former and present components are kindly thanked for their support. I would like to express a special thanks to Luca Leonelli, for his constant advice.

I also thank my colleague Alessandro De Felice for supporting me and sometimes compensating my lack of skills with his competence.

Silvio Sorrentino not only inspired and tutored this work with professional expertise, but also he was a friendly adviser on a personal level. For this, I would like sincerely say thank you.

Finally, a heartfelt thanks to my wife Laura for being constantly on my side.